Unified theory of orientation averaging in X-ray spectroscopies: understanding polarization dependence in a Cartesian tensor approach

Sihan Zhang
MaMaSELF^2 Course, Université de Montpellier, Place Eugène Bataillon, 34090 Montpellier, France and ESRF - The European Synchrtron, 71 Avenue des Martyrs, 38043 Grenoble, France

Oana Bunău, Marius Retegan, and Pieter Glatzel
ESRF - The European Synchrtron, 71 Avenue des Martyrs, 38043 Grenoble, France
(Dated: March 16, 2026)

X-ray absorption spectroscopy (XAS) and resonant inelastic X-ray scattering (RIXS) are powerful probes of electronic structure owing to their chemical and orbital selectivity. For powder samples, however, interpreting RIXS spectral intensities remains challenging as the measured signal is an average over all orientations. Existing theoretical treatments rely largely on spherical-tensor formalisms, which often involve complex derivations and case-specific analyses. Meanwhile, recent advances in quantum-chemistry methods have made the evaluation of transition tensors in Cartesian coordinates both accurate and straightforward. Here, we present a general theoretical framework that translates Cartesian transition tensors into physically meaningful, orientation-averaged intensities for powder samples. The formalism allows predicting angular and polarization dependences *ab initio* for both XAS and RIXS and is extendable to other spectroscopies. The resulting predictions show excellent agreement with RIXS experimental data at the Ce L_3 edge.

arXiv:2603.12355v1 [cond-mat.mtrl-sci] 12 Mar 2026

I. INTRODUCTION

X-ray absorption spectroscopy (XAS) and resonant inelastic X-ray scattering (RIXS) are mature synchrotron radiation techniques that offer a unique insight into the electronic structure at the site of the absorbing species [1, 2]. In particular, high-energy-resolution fluorescence-detected XAS (HERFD-XAS), which is in fact a specific cut in the RIXS plane, is now an established technique for studying the electronic structure of 3d and 4d transition metals [3–7], including under *in situ* and *operando* conditions [8–11], as well as in lanthanide and actinide compounds [12–16].

Beyond the chemical and orbital selectivity inherent to X-ray spectroscopies, photon-in - photon-out techniques such as RIXS provide enhanced control through the choice of incident and emitted polarization as well as the scattering geometry. However, interpretation of such measurements is often qualitative, commonly relying on comparisons to spectra taken on known references. In experimental studies of catalysis and electrochemistry, samples are typically powders [17] providing high surface area and reproducible preparation for spectroscopy and performance measurements. This introduces two major challenges for computing first-principles RIXS spectra of powder samples and for achieving quantitative interpretation of experimental data.

First, it is difficult to reconcile an accurate description of covalency with the inclusion of multiplet effects, arising from electron–electron and electron–core-hole interactions [18, 19]. Established electronic-structure calculation methods such as density functional theory (DFT) can effectively describe band structure but fail to describe strongly correlated systems, as well as the interaction of the atomic-like states (e.g. f) with the localized hole involved in the spectroscopy. Conversely, multiplet ligand field theory [19] or the single impurity Anderson model [19] can accurately capture these interactions, but they require adjustable parameters. The problem can be tackled *ab-initio* by multiconfigurational wavefunction–based quantum-chemistry methods, for example OpenMolcas [20] and ORCA [21], provided sufficiently large cluster models are employed [20–23]. The codes typically output transition tensors in Cartesian form, which constitutes a further practical consideration motivating our work. Although the Cartesian tensor formulation of X-ray spectroscopy is well established [24, 25], powder averages for two photon processes are not implemented in calculations packages. Altogether, establishing a general and universal framework that connects Cartesian transition tensors to orientation-averaged intensities has become increasingly important.

Second, because most studied samples are powders, orientation averaging for a general symmetry is required, whereas previous studies of polarization and angular dependence have focused primarily on single crystals [26–32] or on highly symmetric systems [33]. Several approaches have been proposed to compute orientation-averaged spectra [34–36]. These methods begin by projecting transition tensors onto a spherical basis and then applying group representation theory. Recent developments using this strategy provide a full solution, i.e. orientation averages are expressed as linear combinations of fundamental spectra obtained within the electric dipole (E1E1) approximation for all point-symmetry groups [37, 38]. However, these approaches cannot easily be extended to higher-order multipole contributions, due to the large number of terms involved (3^6 for E2E1 compared to 3^4 for E1E1).

This work presents a general framework for calculating orientation-averaged transition intensities of linearly polarized X-rays and provides a unified description of

TABLE I. Notation used throughout the paper.

Symbol	Meaning
$\Re(a)$	Real part
$\Im(a)$	Imaginary part
$\mathrm{Tr}(\mathbf{A})$	Trace
$\mathbf{A}^\dagger$	Hermitian adjoint
$\mathbf{A}^*$, a^*	Complex conjugate
$\mathbf{A}^\mathrm{T}$, a^*	Transpose
$\mathbf{A}{:}\mathbf{B}$	Tensor contraction: $\sum_{ijk\ldots} A_{ijk\ldots}B_{ijk\ldots}$
$\mathbf{A}\otimes\mathbf{B}$	Tensor product
$\mathbf{D}$, D_i	Rank-1 dipole (E1) transition tensor
$\boldsymbol{\mathcal{D}}$, $\mathcal{D}_{ij}$	$\boldsymbol{\mathcal{D}}=\mathbf{D}^*\otimes\mathbf{D}$, first order rank-2 (E1) tensor
$\mathbf{Q}$, Q_{ij}	Rank-2 quadrupole (E2) transition tensor
$\boldsymbol{\mathcal{R}}$, $\mathcal{R}_{ijk}$	$\boldsymbol{\mathcal{R}}=\mathbf{D}^*\otimes\mathbf{Q}$ rank-3 E1E2 interference tensor
$\boldsymbol{\mathcal{Q}}$, $\mathcal{Q}_{ijkl}$	$\boldsymbol{\mathcal{Q}}=\mathbf{Q}^*\otimes\mathbf{Q}$, first order rank-4 (E2) tensor
$\mathbf{M}$, M_{ij}	second order rank-2 (E1E1) tensor
$\mathbf{S}$, S_{ijk}	second order rank-3 (E2E1) tensor

angular and polarization dependence in XAS and RIXS processes.

Section II introduces the theoretical framework and the key mathematical foundations. We explicitly separate the experimental geometry (polarizations and wavevector orientations) from the sample geometry.

Section III derives the orientation-averaged expressions for XAS and RIXS in terms of Cartesian tensors within a unified formalism. For scattering processes, we consider the particular case of the fundamental in-plane (π) and out-of-plane (σ) polarization configurations and show an analogy with the classical diffraction limit. Some of the results are original—most notably the powder averages for scattering processes—while others, such as the powder average of quadrupolar absorption or the lack of dipole-quadrupole interference contribution in powders, are already known and serve to validate the robustness of our theoretical framework.

Section IV presents an application to experimentally measured core-to-core $2p3d$ and valence-to-core RIXS at the cerium L_3 edge in CeO_2.

A detailed analytical description of the results and the equivalence of the Cartesian and spherical tensor approaches are shown in the appendix.

II. MODEL DESCRIPTION AND MATHEMATICAL BACKGROUND

A. XAS and RIXS cross sections

We start from the exact formulation of the X-ray - matter interaction transition operator $\hat{\mathcal{T}} = (\boldsymbol{\varepsilon}\cdot\boldsymbol{p})e^{i\boldsymbol{k}\cdot\boldsymbol{r}}$ [39] and expand the exponential to linear order in $\boldsymbol{k}\cdot\boldsymbol{r}$ all by taking into account that momentum $\boldsymbol{p}$ and position $\boldsymbol{r}$ operators do not commute [40]:

$$\begin{aligned}\hat{\mathcal{T}} &= \boldsymbol{\varepsilon}\cdot\boldsymbol{p} + \frac{i}{2}\big((\boldsymbol{\varepsilon}\cdot\boldsymbol{p})(\boldsymbol{k}\cdot\boldsymbol{r}) + (\boldsymbol{\varepsilon}\cdot\boldsymbol{r})(\boldsymbol{k}\cdot\boldsymbol{p})\big)\\ &+ \frac{i}{2}\big((\boldsymbol{\varepsilon}\cdot\boldsymbol{p})(\boldsymbol{k}\cdot\boldsymbol{r}) - (\boldsymbol{\varepsilon}\cdot\boldsymbol{r})(\boldsymbol{k}\cdot\boldsymbol{p})\big) + \mathcal{O}(\boldsymbol{k}\cdot\boldsymbol{r})^2 \quad (1)\end{aligned}$$

The first term in Eq. 1 corresponds to the electric dipole (E1) transition while the second one, symmetric upon exchanging $\boldsymbol{r}$ and $\boldsymbol{p}$, is the electric quadrupole (E2). The last linear order term is of magnetic nature (resulting in an antisymmetric tensor) and therefore is not further considered.

From a more practical side, we aim at an alternative expression of the electric transition operator based on $\boldsymbol{r}$ only (instead of $\boldsymbol{r}$ and $\boldsymbol{p}$). For this we rely on the standard commutator relations with the Hamiltonian $\mathcal{H}$ (m is the electron mass):

$$\boldsymbol{p} = \frac{m}{i\hbar}[\boldsymbol{r},\mathcal{H}] \quad (2)$$

and

$$(\boldsymbol{p}\otimes\boldsymbol{r} + \boldsymbol{r}\otimes\boldsymbol{p}) = \frac{m}{i\hbar}[\boldsymbol{r}\otimes\boldsymbol{r},\mathcal{H}] \quad (3)$$

with which:

$$\langle f|\,\boldsymbol{\varepsilon}\cdot\boldsymbol{p}\,|g\rangle = i\frac{m}{\hbar}(E_f - E_g)\,\langle f|\,\boldsymbol{\varepsilon}\cdot\boldsymbol{r}\,|g\rangle = im\omega\,\langle f|\,\boldsymbol{\varepsilon}\cdot\boldsymbol{r}\,|g\rangle \quad (4)$$

This describes the E1 transition from an initial electronic state $|g\rangle$ of energy E_g to final state $|f\rangle$ of energy E_f upon absorbing a photon of energy $\hbar\omega$. For the E2 terms:

$$\begin{aligned}&\langle f|\,(\boldsymbol{\varepsilon}\cdot\boldsymbol{p})(\boldsymbol{k}\cdot\boldsymbol{r}) + (\boldsymbol{\varepsilon}\cdot\boldsymbol{r})(\boldsymbol{k}\cdot\boldsymbol{p})\,|g\rangle\\ =\ &\langle f|\,(\boldsymbol{\varepsilon}\otimes\boldsymbol{k}){:}(\boldsymbol{p}\otimes\boldsymbol{r} + \boldsymbol{r}\otimes\boldsymbol{p})\,|g\rangle\\ =\ &i\frac{m}{\hbar}(E_f - E_g)\,\langle f|\,(\boldsymbol{\varepsilon}\otimes\boldsymbol{k}){:}(\boldsymbol{r}\otimes\boldsymbol{r})\,|g\rangle\\ =\ &im\omega\,\langle f|\,(\boldsymbol{\varepsilon}\cdot\boldsymbol{r})(\boldsymbol{k}\cdot\boldsymbol{r})\,|g\rangle \quad (5)\end{aligned}$$

From Eqs. 1, 4 and 5 we obtain the transition operator form used in this work, containing electrical terms only:

$$\hat{\mathbf{T}} = \boldsymbol{\varepsilon}\cdot\boldsymbol{r} + \frac{i}{2}(\boldsymbol{\varepsilon}\cdot\boldsymbol{r})(\boldsymbol{k}\cdot\boldsymbol{r}) + \mathcal{O}(\boldsymbol{k}\cdot\boldsymbol{r})^2 \quad (6)$$

where the first term corresponds to the electric dipole (E1) transition, and the second term corresponds to the electric quadrupole (E2) transition.

XAS is a one-photon absorption process and is therefore described to first order in perturbation theory. Using Fermi's golden rule the XAS cross section reads

$$\sigma_{\mathrm{XAS}}(\hbar\omega) = 4\pi^2\alpha_{\mathrm{fs}}\hbar\omega\sum_{|f\rangle}|\,\langle f|\,\hat{\mathbf{T}}\,|g\rangle\,|^2\delta(E_f - E_g - \hbar\omega) \quad (7)$$

in units of $[L^2]$ with α_{fs} the fine-structure constant [39].

RIXS is a two-step scattering process (absorption followed by emission) described in the second order of per-

turbation theory [39, 41] with cross section:

$$\sigma_{\mathrm{RIXS}} = \frac{\alpha_{\mathrm{fs}}^2\hbar^2}{c^2}\omega_i\omega_o^3\sum_{|f\rangle}\left|\sum_{|n\rangle}\frac{\langle f|\,\hat{\mathbf{T}}_o^\dagger\,|n\rangle\,\langle n|\,\hat{\mathbf{T}}_i\,|g\rangle}{E_n - E_g - \hbar\omega_i + i\Gamma_n}\right|^2 \times\delta(E_f - E_g - \hbar(\omega_i - \omega_o)) \quad (8)$$

in units of $[L^2]/[E]$. Here $\hat{\mathbf{T}}_i$ ($\hat{\mathbf{T}}_o$) is the transition operator corresponding to the absorption (emission) process of the incoming (outgoing) photon of energy $\hbar\omega_i$ ($\hbar\omega_o$). Note that prefactors in Eqs. 7 and 8 are specific to the chosen transition operator form in Eq. 6.

B. Orientation averaging and tensor-integral reduction

In their standard form, Eqs. 7 and 8 are not well suited for analyzing orientation dependence. To address this, we seek an alternative representation that cleanly separates the angular contributions originating from the experimental geometry (i.e., the orientations of the polarization vectors and wavevectors) from those inherent to the sample, encoded in the transition matrix elements. The latter obey the symmetry constraints of the point group of the absorbing atom and therefore possess their own intrinsic angular dependence. To make this separation explicit, the cross sections can be recast as a series of tensor contractions:

$$\begin{aligned}\sigma &= |(\boldsymbol{v}_1\cdot\mathbf{D}_1)\cdots(\boldsymbol{v}_k\cdot\mathbf{D}_k)|^2\\ &= (\boldsymbol{v}_1^*\otimes\cdots\otimes\boldsymbol{v}_k^*\otimes\boldsymbol{v}_1\otimes\cdots\otimes\boldsymbol{v}_k)\\ &\quad :(\mathbf{D}_1^*\otimes\cdots\otimes\mathbf{D}_k^*\otimes\mathbf{D}_1\otimes\cdots\otimes\mathbf{D}_k)\end{aligned} \quad (9)$$

where we used the notations explicitly stated in Table I and $\boldsymbol{v}$ denotes vectors such as polarization $\boldsymbol{\varepsilon}$ and wave vector $\boldsymbol{k}$.

Thanks to Eq. 9 the cross section at any symmetry-equivalent site can be obtained simply by applying the corresponding transformation $\mathbf{R}$ to the transition tensors.

$$\sigma^{(\mathbf{R})} = (\boldsymbol{v}_1^*\otimes\cdots\otimes\boldsymbol{v}_k):((\mathbf{R}\mathbf{D}_1)^*\otimes\cdots\otimes\mathbf{R}\mathbf{D}_k) \quad (10)$$

For non-magnetic and non-chiral materials, the cross section of a powder sample is obtained by averaging over all possible crystallite orientations, i.e., over the SO(3) rotation group:

$$\langle\sigma\rangle_{\mathbf{R}} = \int_{SO(3)}\sigma^{(\mathbf{R})}\,d\mathbf{R} \quad (11)$$

with $\mathbf{R}$ an orthogonal rotation matrix.

Whereas for a single crystal one must explicitly sum the contributions from all symmetry-equivalent sites of the absorbing atom, in a powder these contributions are automatically included by the rotational averaging. Indeed, the isotropic components associated with two symmetry-related sites connected by a point-group operation g are identical:

$$\int_{SO(3)}\sigma^{(\mathbf{R})}\,d\mathbf{R} \equiv \int_{SO(3)}\sigma^{(\mathbf{Rg})}\,d\mathbf{R} \quad (12)$$

where $\sigma^{(g)}$ is the result of applying the symmetry operation g to the transition tensors. Thus, once the transition tensor is constructed for the minimal set of sites that generate all others via real-space symmetry operations, no additional accounting for symmetry-equivalent atomic positions is required in the powder average. For samples containing non-equivalent atomic sites, the orientational averages must be evaluated separately for each site and subsequently summed.

Direct evaluation of the integral in Eq. 11 is generally impractical because the number of terms grows rapidly with the tensor rank. A more tractable strategy is to exploit combinatorial methods. In particular, it is known that the rotational average of any even-rank Cartesian tensor over SO(3) can be written as a linear combination of products of Kronecker deltas, with coefficients determined solely by combinatorial factors [42, 43].

To illustrate the procedure, consider a rank-4 Cartesian tensor $\boldsymbol{\mathcal{Q}}$. Its rotational average admits an expansion in the basis formed by all independent products of Kronecker deltas:

$$\langle\boldsymbol{\mathcal{Q}}\rangle = \alpha\,A_{ijkl} + \beta\,B_{ijkl} + \gamma\,C_{ijkl} \quad (13)$$

where:

$$\begin{aligned}A_{ijkl} &= \delta_{ik}\delta_{jl}\\ B_{ijkl} &= \delta_{ij}\delta_{kl}\\ C_{ijkl} &= \delta_{il}\delta_{jk}\end{aligned} \quad (14)$$

The expansion coefficients α, β, and γ can be obtained by solving the linear system:

$$\begin{bmatrix}\mathbf{A}{:}\mathbf{A} & \mathbf{A}{:}\mathbf{B} & \mathbf{A}{:}\mathbf{C}\\ \mathbf{B}{:}\mathbf{A} & \mathbf{B}{:}\mathbf{B} & \mathbf{B}{:}\mathbf{C}\\ \mathbf{C}{:}\mathbf{A} & \mathbf{C}{:}\mathbf{B} & \mathbf{C}{:}\mathbf{C}\end{bmatrix}\begin{bmatrix}\alpha\\ \beta\\ \gamma\end{bmatrix} = \begin{bmatrix}\mathbf{A}{:}\boldsymbol{\mathcal{Q}}\\ \mathbf{B}{:}\boldsymbol{\mathcal{Q}}\\ \mathbf{C}{:}\boldsymbol{\mathcal{Q}}\end{bmatrix} \quad (15)$$

The matrix on the left-hand side is called the Gram matrix. In particular:

$$G_{ij} = \begin{cases}\sum_{ijkl}(\delta_{ij}\delta_{kl})(\delta_{ij}\delta_{kl}) = \sum_{ij}1 = 9 & i = j\\ \sum_{ijkl}(\delta_{ij}\delta_{kl})\,(\delta_{ik}\delta_{jl}) = \sum_{i}\delta_{ii} = 3 & i \neq j\end{cases} \quad (16)$$

Subsequently:

$$\begin{bmatrix}\alpha\\ \beta\\ \gamma\end{bmatrix} = \frac{1}{30}\begin{bmatrix}4 & -1 & -1\\ -1 & 4 & -1\\ -1 & -1 & 4\end{bmatrix}\sum_{ijkl}\begin{bmatrix}\delta_{ik}\delta_{jl}\\ \delta_{ij}\delta_{kl}\\ \delta_{il}\delta_{jk}\end{bmatrix}\mathcal{Q}_{ijkl} \quad (17)$$

Formally the same procedure can be applied to obtain the rotational average of a rank-2 tensor $\boldsymbol{\mathcal{D}}$:

$$\langle\boldsymbol{\mathcal{D}}\rangle = \alpha\,\delta_{ij} \quad (18)$$

where the Gram matrix reduces to a scalar and:

$$\alpha = \frac{1}{3}\sum_{ij}\delta_{ij}\mathcal{D}_{ij} = \frac{1}{3}\,\mathrm{Tr}(\boldsymbol{\mathcal{D}}) \tag{19}$$

For higher-order tensors (rank 6 and above), the associated Gram matrices have been computed by D. L. Andrews [44, 45], and these results will be used directly in the calculations that follow.

III. ORIENTATION AVERAGES FOR X-RAY SPECTROSCOPY

The rotational averages $\langle\boldsymbol{\mathcal{D}}\rangle$ and $\langle\boldsymbol{\mathcal{Q}}\rangle$ involve only the transition tensors. For the evaluation of spectroscopic observables, however, the experimental geometry must be included as in Eq. 9.

A. XAS

We start with the simplest case, namely the powder average of the E1 XAS term. Using Eqs. 18 and 19, we recover the well-known result:

$$\begin{aligned}\langle\sigma^{\mathrm{E1}}_{\mathrm{XAS}}\rangle &= \sum_{ij}\varepsilon_i^*\,\langle\boldsymbol{\mathcal{D}}\rangle\,\varepsilon_j \\ &= \frac{1}{3}|\boldsymbol{\varepsilon}|^2\,\mathrm{Tr}\,(\boldsymbol{\mathcal{D}}) = \frac{1}{3}|\boldsymbol{\varepsilon}|^2|\mathbf{D}|^2\end{aligned} \tag{20}$$

where, formally, one may work either with the rank-2 E1 tensor $\boldsymbol{\mathcal{D}} = \mathbf{D}^*\otimes\mathbf{D}$ or directly with the rank-1 E1 transition vector $\mathbf{D}$ defined as $\langle f|\,\boldsymbol{r}\,|g\rangle$.

The E2 XAS term is associated to a rank-4 tensor. Its orientation average is:

$$\langle\sigma^{\mathrm{E2}}_{\mathrm{XAS}}\rangle = \sum_{ijkl}\varepsilon_i^*k_j^*\,\langle\boldsymbol{\mathcal{Q}}\rangle\,\varepsilon_k k_l \tag{21}$$

and eventually from Eq. 17:

$$\langle\sigma^{\mathrm{E2}}_{\mathrm{XAS}}\rangle = \frac{1}{30}\begin{bmatrix}|\boldsymbol{\varepsilon}|^2|\boldsymbol{k}|^2\\ |\boldsymbol{\varepsilon}\cdot\boldsymbol{k}|^2\\ |\boldsymbol{\varepsilon}^*\cdot\boldsymbol{k}|^2\end{bmatrix}^{\mathrm{T}}\begin{bmatrix}4&-1&-1\\-1&4&-1\\-1&-1&4\end{bmatrix}\sum_{ij}\begin{bmatrix}\mathcal{Q}_{ijij}\\ \mathcal{Q}_{iijj}\\ \mathcal{Q}_{ijji}\end{bmatrix}$$

For convenience we choose to work with the rank-2 E2 tensors $\mathbf{Q} = \langle f|\,\boldsymbol{r}\otimes\boldsymbol{r}\,|g\rangle$. $\mathbf{Q}$, a symmetric tensor by construction ($Q_{ij} = Q_{ji}$).

With this the E2 XAS isotropic signal reads:

$$\langle\sigma^{\mathrm{E2}}_{\mathrm{XAS}}\rangle = \frac{1}{30}\begin{bmatrix}|\boldsymbol{\varepsilon}|^2|\boldsymbol{k}|^2\\ |\boldsymbol{\varepsilon}\cdot\boldsymbol{k}|^2\\ |\boldsymbol{\varepsilon}^*\cdot\boldsymbol{k}|^2\end{bmatrix}^{\mathrm{T}}\begin{bmatrix}4&-1&-1\\-1&4&-1\\-1&-1&4\end{bmatrix}\sum_{ij}\begin{bmatrix}Q_{ij}^*Q_{ij}\\ Q_{ii}^*Q_{jj}\\ Q_{ij}^*Q_{ji}\end{bmatrix}$$

Since in first order processes the polarization $\boldsymbol{\varepsilon}$ is perpendicular to the wavevector $\boldsymbol{k}$, the above reduces to:

$$\begin{aligned}\langle\sigma^{\mathrm{E2}}_{\mathrm{XAS}}\rangle &= \frac{1}{30}|\boldsymbol{\varepsilon}|^2|\boldsymbol{k}|^2\times \\ &\times\left(4\sum_{ij}Q_{ij}^*Q_{ij} - \sum_{ij}Q_{ii}^*Q_{jj} - \sum_{ij}Q_{ij}^*Q_{ji}\right)\end{aligned} \tag{22}$$

We use $\mathbf{Q}$'s symmetry property to further simplify to:

$$\langle\sigma^{\mathrm{E2}}_{\mathrm{XAS}}\rangle = \frac{1}{30}|\boldsymbol{\varepsilon}|^2|\boldsymbol{k}|^2\left(3\,\mathrm{Tr}(\mathbf{Q}^\dagger\mathbf{Q}) - |\,\mathrm{Tr}(\mathbf{Q})|^2\right)$$

with $\mathrm{Tr}(\mathbf{Q}^\dagger\mathbf{Q}) = \sum_{ij}Q_{ij}^*Q_{ij}$, $|\,\mathrm{Tr}(\mathbf{Q})|^2 = \sum_{ij}Q_{ii}^*Q_{jj}$. With explicit cartesian indices:

$$\begin{aligned}\langle\sigma^{\mathrm{E2}}_{\mathrm{XAS}}\rangle &= \frac{|\boldsymbol{\varepsilon}|^2|\boldsymbol{k}|^2}{15}\left(|Q_{xx}|^2 + 3|Q_{xy}|^2 - \Re(Q_{xx}^*Q_{yy})\right) \\ &+ \text{ cyclic permutations}\end{aligned} \tag{23}$$

The result above is identical to the one in reference [46], provided we expand in four-index form:

$$\begin{aligned}\langle\sigma^{\mathrm{E2}}_{\mathrm{XAS}}\rangle &= \frac{|\boldsymbol{\varepsilon}|^2|\boldsymbol{k}|^2}{15}(\mathcal{Q}_{xxxx} + 3\mathcal{Q}_{xyxy} - \mathcal{Q}_{xxyy}) \\ &+ \text{ cyclic permutations}\end{aligned} \tag{24}$$

Equations 20 and 23 make it evident that the E1 and E2 contributions to XAS in a powder sample exhibit no dependence on either wavevector orientation or polarization.

Under specific conditions, E1 and E2 transitions may interfere:

$$\begin{aligned}\sigma^{\mathrm{E1+E2}}_{\mathrm{XAS}} &= |\,\langle f|\,\boldsymbol{\varepsilon}\cdot\boldsymbol{r} + \frac{i}{2}(\boldsymbol{\varepsilon}\cdot\boldsymbol{r})(\boldsymbol{r}\cdot\boldsymbol{k})\,|g\rangle\,|^2 \\ &= \sigma^{\mathrm{E1}}_{\mathrm{XAS}} + \frac{1}{4}\sigma^{\mathrm{E2}}_{\mathrm{XAS}} \\ &\quad -\Im(\langle g|\,(\boldsymbol{\varepsilon}\cdot\boldsymbol{r})^*\,|f\rangle\,\langle f|\,(\boldsymbol{\varepsilon}\cdot\boldsymbol{r})(\boldsymbol{r}\cdot\boldsymbol{k})\,|g\rangle)\end{aligned} \tag{25}$$

The last term corresponds to the E1E2 interference contribution, denoted $\sigma^{\mathrm{E1E2}}_{\mathrm{XAS}}$. It involves the $\boldsymbol{\mathcal{R}} = \mathbf{D}^*\otimes\mathbf{Q}$ rank 3 tensor where $\mathcal{R}_{ijk} = \langle g|\,r_i\,|f\rangle\,\langle f|\,r_jr_k\,|g\rangle$. Subsequently the interference term can be written as :

$$\sigma^{\mathrm{E1E2}}_{\mathrm{XAS}} = -\Im\left(\sum_{ijk}\varepsilon_i^*\varepsilon_jk_k\mathcal{R}_{ijk}\right) \tag{26}$$

The orientation average of odd ranked tensors may be evaluated using a procedure analogous to that introduced in Section II B, equally developed in Ref. [44]. For rank 3 tensors, the only isotropic basis is provided by the antisymmetric Levi-Civita symbol ϵ_{ijk}. Accordingly, the orientation average can be expanded as $\langle\mathcal{R}\rangle = \beta\epsilon_{ijk}$ where the expansion coefficient is given by $\beta = \frac{1}{6}\sum_{ijk}\epsilon_{ijk}\mathcal{R}_{ijk}$. This yields

$$\langle\sigma^{\mathrm{E1E2}}_{\mathrm{XAS}}\rangle = -\Im\frac{1}{6}\left(\sum_{ijk}\epsilon_{ijk}\varepsilon_i^*\varepsilon_jk_k\right)\left(\sum_{ijk}\epsilon_{ijk}\mathcal{R}_{ijk}\right) \tag{27}$$

Here, j and k are the two indices of the symmetric E2 tensor $\mathbf{Q}$. The second term of the product in Eq. 27 is a Levi-Civita sum with two switchable indexes, so it must be zero. This is consistent to the known result, namely that the E1E2 interference has no isotropic component and therefore does not contribute to the absorption cross section in powder samples [40, 47].

B. RIXS

1. General formalism

The E1E1 RIXS term is associated to a rank-4 tensor. Its orientation average is:

$$\langle \sigma_{\mathrm{RIXS}}^{\mathrm{E1E1}} \rangle = \sum_{ijkl} \varepsilon_{i,i}^{*} \varepsilon_{o,j} \langle \boldsymbol{\mathcal{Q}} \rangle \varepsilon_{i,k} \varepsilon_{o,l}^{*} \tag{28}$$

with $\boldsymbol{\varepsilon}_i$ ($\boldsymbol{\varepsilon}_o$) the incoming (outgoing) polarization. From this point the derivation is similar to the one of E2 XAS:

$$\langle \sigma_{\mathrm{RIXS}}^{\mathrm{E1E1}} \rangle = \frac{1}{30} \begin{bmatrix} |\boldsymbol{\varepsilon}_o|^2 |\boldsymbol{\varepsilon}_i|^2 \\ |\boldsymbol{\varepsilon}_o^* \cdot \boldsymbol{\varepsilon}_i|^2 \\ |\boldsymbol{\varepsilon}_o \cdot \boldsymbol{\varepsilon}_i|^2 \end{bmatrix}^{\mathrm{T}} \begin{bmatrix} 4 & -1 & -1 \\ -1 & 4 & -1 \\ -1 & -1 & 4 \end{bmatrix} \sum_{ij} \begin{bmatrix} M_{ij}^* M_{ij} \\ M_{ii}^* M_{jj} \\ M_{ij}^* M_{ji} \end{bmatrix}$$

where rank-2 tensor $\mathbf{M}$ is defined as:

$$\begin{aligned} \mathbf{M} &= \sum_n G_n \cdot \mathbf{D}^{ng} \otimes \mathbf{D}^{fn} \\ M_{ij} &= \sum_n \frac{\langle n | r_i | g \rangle \cdot \langle f | r_j | n \rangle}{E_n - E_g - \hbar\omega_i + i\Gamma_n} \end{aligned} \tag{29}$$

with $G_n = 1/(E_n - E_g - \hbar\omega_i + i\Gamma_n)$ the Green function and the relationship between 2- and 4-index tensors is:

$$\mathcal{Q}_{ijkl} = M_{ij}^* M_{kl} \tag{30}$$

For the general form tensor it can be easily shown that:

$$\begin{aligned} \mathrm{Tr}(\mathbf{M}^\dagger \mathbf{M}) &= \sum_{ij} M_{ij}^\dagger M_{ji} = \sum_{ij} M_{ij}^* M_{ij} \\ \mathrm{Tr}(\mathbf{M}^* \mathbf{M}) &= \sum_{ij} M_{ij}^* M_{ji} \\ |\,\mathrm{Tr}(\mathbf{M})|^2 &= \sum_{ij} M_{ii}^* M_{jj} \end{aligned} \tag{31}$$

with which:

$$\begin{aligned} \langle \sigma_{\mathrm{RIXS}}^{\mathrm{E1E1}} \rangle &= \frac{1}{30} \begin{bmatrix} |\boldsymbol{\varepsilon}_o|^2 |\boldsymbol{\varepsilon}_i|^2 \\ |\boldsymbol{\varepsilon}_o^* \cdot \boldsymbol{\varepsilon}_i|^2 \\ |\boldsymbol{\varepsilon}_o \cdot \boldsymbol{\varepsilon}_i|^2 \end{bmatrix}^{\mathrm{T}} \times \\ &\times \begin{bmatrix} 4 & -1 & -1 \\ -1 & 4 & -1 \\ -1 & -1 & 4 \end{bmatrix} \begin{bmatrix} \mathrm{Tr}(\mathbf{M}^\dagger \mathbf{M}) \\ |\,\mathrm{Tr}(\mathbf{M})|^2 \\ \mathrm{Tr}(\mathbf{M}^* \mathbf{M}) \end{bmatrix} \end{aligned} \tag{32}$$

In photon-in photon-out (second order) processes the incident and scattered polarization vectors, $\boldsymbol{\varepsilon}_i$ and $\boldsymbol{\varepsilon}_o$, are not constrained to be orthogonal. This lack of orthogonality is the origin of the angular and polarization dependence that appears in RIXS measurements on powders. This contrasts with the XAS E2 case, where no angular dependence arises because the wavevector is always perpendicular to the polarization. Moreover, Eq. 32 highlights an additional important consequence: when the two polarization vectors are mutually perpendicular, the intensity becomes independent of both angle and polarization. A similar conclusion was reached in Ref. [36].

The intensity for any higher multipole order can be evaluated in a similar way, with the Gram matrix taken from [44, 45]. For higher orders the advantage of 1- and 2-index notations becomes obvious. Let us consider the E2E1 RIXS (E2 in, E1 out), described by a 6-order tensor:

$$\sigma_{\mathrm{RIXS}}^{\mathrm{E2E1}} = \left| \sum_{ijk} \boldsymbol{\varepsilon}_{i,i} k_j \boldsymbol{\varepsilon}_{o,k} S_{ijk} \right|^2 \tag{33}$$

where $\mathbf{S} = \sum_n G_n \cdot \mathbf{Q} \otimes \mathbf{D}$ ($S_{ijk} = Q_{ij} D_k$). Since $\mathbf{Q}$ is a symmetric tensor we have:

$$S_{ijk} = S_{jik} \tag{34}$$

The orientation average of the E2E1 RIXS term is:

$$\langle\sigma^{\mathrm{E2E1}}_{\mathrm{RIXS}}\rangle = \frac{1}{210}\begin{bmatrix}|\boldsymbol{\varepsilon}_o|^2|\boldsymbol{\varepsilon}_i|^2|\boldsymbol{k}_i|^2\\ |\boldsymbol{\varepsilon}_o^*\cdot\boldsymbol{\varepsilon}_i|^2|\boldsymbol{k}_i|^2\\ |\boldsymbol{\varepsilon}_o\cdot\boldsymbol{\varepsilon}_i|^2|\boldsymbol{k}_i|^2\\ |\boldsymbol{\varepsilon}_o^*\cdot\boldsymbol{k}_i|^2|\boldsymbol{\varepsilon}_i|^2\\ |\boldsymbol{\varepsilon}_o\cdot\boldsymbol{k}_i|^2|\boldsymbol{\varepsilon}_i|^2\end{bmatrix}^{\mathrm{T}}\begin{bmatrix}16&-5&-5&-5&-5\\-5&16&-5&2&2\\-5&-5&16&2&2\\-5&2&2&16&-5\\-5&2&2&-5&16\end{bmatrix}\begin{bmatrix}\delta_{ii'}\delta_{jj'}\delta_{kk'}\\ \delta_{ii'}\delta_{jk}\delta_{j'k'}\\ \delta_{ii'}\delta_{jk'}\delta_{j'k}\\ \delta_{ik}\delta_{jj'}\delta_{i'k'}\\ \delta_{ik'}\delta_{jj'}\delta_{i'k}\end{bmatrix}\sum_{ii'jj'kk'}S^*_{i'j'k'}S_{ijk}$$

$$= \frac{1}{210}\begin{bmatrix}|\boldsymbol{\varepsilon}_o|^2|\boldsymbol{\varepsilon}_i|^2|\boldsymbol{k}_i|^2\\ |\boldsymbol{\varepsilon}_o^*\cdot\boldsymbol{\varepsilon}_i|^2|\boldsymbol{k}_i|^2\\ |\boldsymbol{\varepsilon}_o\cdot\boldsymbol{\varepsilon}_i|^2|\boldsymbol{k}_i|^2\\ |\boldsymbol{\varepsilon}_o^*\cdot\boldsymbol{k}_i|^2|\boldsymbol{\varepsilon}_i|^2\\ |\boldsymbol{\varepsilon}_o\cdot\boldsymbol{k}_i|^2|\boldsymbol{\varepsilon}_i|^2\end{bmatrix}^{\mathrm{T}}\begin{bmatrix}16&-5&-5&-5&-5\\-5&16&-5&2&2\\-5&-5&16&2&2\\-5&2&2&16&-5\\-5&2&2&-5&16\end{bmatrix}\begin{bmatrix}\mathrm{Tr}(\mathbf{Q}^\dagger\mathbf{Q})|\mathbf{D}|^2\\ |\mathbf{QD}|^2\\ |\mathbf{QD}^*|^2\\ |\mathbf{Q}^{\mathrm{T}}\mathbf{D}|^2\\ |\mathbf{Q}^{\mathrm{T}}\mathbf{D}^*|^2\end{bmatrix} \tag{35}$$

The orientation averaged E1E2 RIXS can be constructed in a similar way. The corresponding result consists in interchanging ε_i and ε_o in Eq. 35 above.

2. *Projections onto polarization channels*

In the previous section, we derived the general expression for the RIXS scattering cross section corresponding to arbitrary incident and emitted polarizations. In practice, however, this formulation has limited direct applicability, since most experiments employ linearly polarized incident light and polarization-insensitive detection. Consequently, the intensity must be projected onto the polarization configuration dictated by the experimental geometry.

The relevant angles and directions are shown in Fig. 1. The angle between the incident and scattered wavevectors, $\boldsymbol{k}_i$ and $\boldsymbol{k}_o$, is α, the scattering angle.

For a fixed scattering geometry, the incident and outgoing polarization vectors can be uniquely expressed in terms of their σ (perpendicular) and π (parallel) components with respect to the scattering plane spanned by $\boldsymbol{k}_i$ and $\boldsymbol{k}_o$:

$$\boldsymbol{\varepsilon}_{i,o} = |\boldsymbol{\varepsilon}_{i,o}|\cdot(\hat{\boldsymbol{\varepsilon}}^{\pi}_{i,o}\cos\phi_{i,o} + \hat{\boldsymbol{\varepsilon}}^{\sigma}_{i,o}\sin\phi_{i,o}) \tag{36}$$

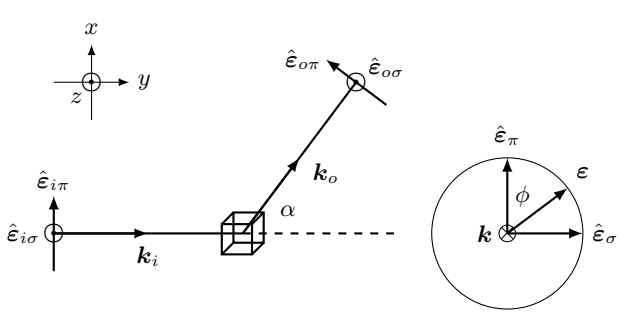

FIG. 1. Photon-in photon-out scattering geometry

a. E1E1 RIXS By combining Eq. 32 and Eq. 36, the orientation average of the E1E1 RIXS intensity for linear polarizations is (up to a multiplicative factor):

$$I_{\mathrm{E1E1}}(\alpha,\phi_i,\phi_o) = a + b(\sin\phi_i\sin\phi_o + \cos\phi_i\cos\phi_0\cos\alpha)^2 \tag{37}$$

where

$$\begin{aligned} a &= \frac{1}{30}|\boldsymbol{\varepsilon}_i|^2|\boldsymbol{\varepsilon}_o|^2 \\ &\quad (4\,\mathrm{Tr}(\mathbf{M}^\dagger\mathbf{M}) - |\,\mathrm{Tr}(\mathbf{M})|^2 - \mathrm{Tr}(\mathbf{M}^*\mathbf{M})) \\ b &= \frac{1}{30}|\boldsymbol{\varepsilon}_i|^2|\boldsymbol{\varepsilon}_o|^2 \\ &\quad (-2\,\mathrm{Tr}(\mathbf{M}^\dagger\mathbf{M}) + 3|\,\mathrm{Tr}(\mathbf{M})|^2 + 3\,\mathrm{Tr}(\mathbf{M}^*\mathbf{M})) \end{aligned} \tag{38}$$

By projecting on the polarization channels σ ($\phi = \pi/2$) and π ($\phi = 0$):

$$\begin{aligned} I^{\sigma\sigma}_{\mathrm{E1E1}}(\alpha) &= a + b \\ I^{\sigma\pi}_{\mathrm{E1E1}}(\alpha) &= I^{\pi\sigma}_{\mathrm{E1E1}}(\alpha) = a \\ I^{\pi\pi}_{\mathrm{E1E1}}(\alpha) &= a + b\cos^2\alpha \end{aligned} \tag{39}$$

one can see the angular dependence is lost for σ-polarized incident light and for the crossed polarization channels.

When the outgoing polarization is not detected one must average over all ϕ_o values:

$$I(\alpha,\phi_i) = \frac{1}{2\pi}\int_0^{2\pi} I(\alpha,\phi_i,\phi_o)\,d\phi_o \tag{40}$$

In particular, from Eq. 37:

$$I_{\mathrm{E1E1}}(\alpha,\phi_i) = a + \frac{1}{2}b(\sin^2\phi_i + \cos^2\phi_i\cos^2\alpha) \tag{41}$$

Subsequently, for σ and π incident polarizations:

$$\begin{aligned} I^{\sigma}_{\mathrm{E1E1}}(\alpha) &= a + \frac{1}{2}b \\ I^{\pi}_{\mathrm{E1E1}}(\alpha) &= a + \frac{1}{2}b\cos^2\alpha \end{aligned} \tag{42}$$

b. E2E1 and E1E2 RIXS By plugging Eq. 36 into Eq. 35, the orientation average of the E2E1 and E1E2 RIXS read:

$$\begin{aligned} I_{\mathrm{E2E1}}(\alpha,\phi_i,\phi_o) &= a + 2b\cos^2\phi_o\sin^2\alpha \\ &+ 2b(\sin\phi_i\sin\phi_o + \cos\phi_i\cos\phi_0\cos\alpha)^2 \end{aligned}$$

$$I_{\mathrm{E1E2}}(\alpha,\phi_i,\phi_o) = a + 2b\cos^2\phi_i\sin^2\alpha + 2b(\sin\phi_i\sin\phi_o + \cos\phi_i\cos\phi_0\cos\alpha)^2 \quad (43)$$

where

$$\begin{aligned} a &= \frac{1}{105}|\boldsymbol{\varepsilon}_{\mathrm{E1}}|^2|\boldsymbol{\varepsilon}_{\mathrm{E2}}|^2|\boldsymbol{k}_{\mathrm{E2}}|^2 \\ &\quad (8\,\mathrm{Tr}(\mathbf{Q}^\dagger\mathbf{Q})|\mathbf{D}|^2 - 5|\mathbf{QD}|^2 - 5|\mathbf{QD}^*|^2) \\ b &= \frac{1}{42}|\boldsymbol{\varepsilon}_{\mathrm{E1}}|^2|\boldsymbol{\varepsilon}_{\mathrm{E2}}|^2|\boldsymbol{k}_{\mathrm{E2}}|^2 \\ &\quad (-2\,\mathrm{Tr}(\mathbf{Q}^\dagger\mathbf{Q})|\mathbf{D}|^2 + 3|\mathbf{QD}|^2 + 3|\mathbf{QD}^*|^2) \end{aligned} \quad (44)$$

By projecting on the individual channels:

$$\begin{aligned} I^{\sigma\sigma}_{\mathrm{E2E1}} &= I^{\pi\pi}_{\mathrm{E2E1}} = I^{\sigma\sigma}_{\mathrm{E1E2}} = I^{\pi\pi}_{\mathrm{E1E2}} = a + 2b \\ I^{\sigma\pi}_{\mathrm{E2E1}} &= I^{\pi\sigma}_{\mathrm{E1E2}} = a + 2b\sin^2\alpha \\ I^{\pi\sigma}_{\mathrm{E2E1}} &= I^{\sigma\pi}_{\mathrm{E1E2}} = a \end{aligned} \quad (45)$$

When the outgoing polarization is not detected:

$$\begin{aligned} I_{\mathrm{E2E1}}(\alpha,\phi_i) &= a + b(1+\sin^2\phi_i\sin^2\alpha) \\ I_{\mathrm{E1E2}}(\alpha,\phi_i) &= a + b(1+\cos^2\phi_i\sin^2\alpha) \end{aligned} \quad (46)$$

In particular, for σ and π incident polarizations:

$$\begin{aligned} I^{\sigma}_{\mathrm{E2E1}}(\alpha) &= I^{\pi}_{\mathrm{E1E2}}(\alpha) = a + b(1+\sin^2\alpha) \\ I^{\pi}_{\mathrm{E2E1}}(\alpha) &= I^{\sigma}_{\mathrm{E1E2}}(\alpha) = a + b \end{aligned} \quad (47)$$

3. *Scattering from spherically symmetric states*

Consider the non-resonant scattering cross section σ_{Th}, i.e. the Thomson term. For linearly polarized light:

$$\sigma_{\mathrm{Th}}(q) = r_0^2|f_0(q)|^2|\hat{\boldsymbol{\varepsilon}}_o\cdot\hat{\boldsymbol{\varepsilon}}_i|^2 \quad (48)$$

where r_0 is the classical electron radius, q the momentum transfer and $f_0(q)$ the atomic form factor. Thomson scattering originates from the spherically symmetric part of the electronic charge density and is therefore rotational invariant. Similarly, when the electron states f and g are spherically symmetric we retrieve a special case of Eq. 32 where the scattering tensor is:

$$\mathbf{M} \propto \begin{bmatrix} 1 & 0 & 0 \\ 0 & 1 & 0 \\ 0 & 0 & 1 \end{bmatrix} \quad (49)$$

This will give a coefficient $a = 0$ in Eq. 38 with which the angular dependence in Eq. 37 becomes Thomson-like, i.e. similar to Eq. 48. Furthermore, like in the Thomson scattering, the crossed polarization $\sigma\pi$ and $\pi\sigma$ terms in Eq. 39 are forbidden.

Here we have treated the resonant scalar scattering and Thomson scattering on equal footing, as they have identical tensor structures. Nevertheless the classical diffraction limit cannot rigorously be retrieved from our theory, as they stem from different Hamiltonian terms [39].

IV. APPLICATION

We apply our method to study the angular dependence of two types of RIXS processes at the L_3 edge of CeO_2. The first is core-to-core (ctc) $2p3d$ RIXS, in particular L_3M_5 RIXS (the $L_{\alpha1}$ line, i.e. the $3d_{5/2} \to 2p_{3/2}$ resonant emission) and L_3M_4 RIXS (the $L_{\alpha2}$ line, i.e. $3d_{3/2} \to 2p_{3/2}$). The second is valence-to-core (vtc) RIXS, corresponding to $2p_{3/2} \to 5d$ transitions.

A. Methods

1. *Experiment setup*

The measurements were performed at beamline ID26 of the European Synchrotron Research Facility, using a spectrometer set in a vertical Rowland geometry [48] with sample, detector and five crystal analyzers arranged on 1m radius circles. The round analyzer crystals have a diameter of 100mm. The incoming X-ray polarization is horizontal, parallel to the scattering plane (π incident polarization) and no polarization analysis was performed. Spectra were collected by displacing a pixel detector (Dectris Pilatus 100k) by 40 mm from the nominal focusing condition outside the Rowland circle. In this configuration, each analyzer produces a distinct spot on the detector allowing 5 scattering angles to be recorded simultaneously (Fig. 2).

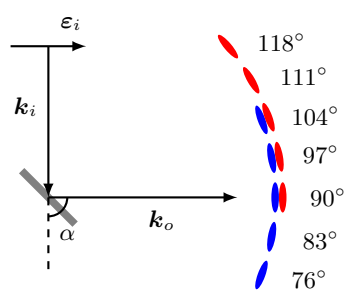

FIG. 2. Positioning of the analyzer crystals with respect to the sample (blue for the vtc measurement, red for ctc).

The incident energy was scanned using a Si(311) double crystal monochromator. The beam size was 0.2 mm (horizontal) x 0.1 (vertical) and the sample surface was oriented at approximately 45 degrees relative to the incoming beam. The rotation of the (powder) sample does not affect the angular distribution of the intensity, beyond self-absorption effects. RIXS planes were acquired by continuously scanning the monochromator energy for each analyzer position, while the undulator gap was tuned to maximize the incident photon flux on the first harmonic. Higher harmonics were rejected by total reflection on Si mirrors inclined at 2.5 mrad with respect to the incident beam. The incident intensity used for normalization was monitored in real time with a photo diode

operating in backscattering geometry. One-dimensional cuts of the RIXS planes were obtained by binning the data directly, without applying any smoothing or interpolation procedures [49].

The Ge(333) reflection at 84° Bragg angle was used for the vtc RIXS measurements, yielding an overall energy resolution of 0.5 eV, defined as the full width at half maximum of the elastic line. The analyzer crystals were arranged in a symmetric configuration, with the central analyzer positioned at a scattering angle of 90° and the remaining analyzers placed at 90° ± 7° and 90° ± 14° (Fig. 2). Note that the diameter of an analyzer crystal covers an angle of ≈ 6.4°. For measurements of the $2p3d$ RIXS the Ge(331) reflection at 81° was used, providing a total energy resolution of 0.8 eV. In this case, the spectrometer was rotated so that the analyzers were set to cover a 28° range, from 90° to 118° (Fig. 2). The incoming energy was calibrated by measuring the K absorption edge of a Ti foil. The energy calibration of the scattered X-rays is based on the geometric alignment of the spectrometer components. In the case of vtc RIXS, the elastic scattering is used to achieve absolute calibration of the energy transfer.

The CeO_2 powder was purchased commercially and pressed to a pellet. No radiation damage was noticed during the experiment.

2. Computational method

Transition tensors were calculated by OpenMolcas v25.06 [20, 50]. The embedded cluster model of CeO_2 was constructed based on crystal structures of ICSD 88759 [51]. Zone 1 (full-basis atoms) consisted of a Ce-centered ${CeO_8}^{12-}$ cluster. Zone 2 contained 400 fixed point charges, while Zone 3 contained 1000 variable point charges used to balance the electrostatic potential of Zones 1 and 2. The point charges were generated using the Ewald program [52, 53], based on a search within a $12 \times 12 \times 12$ supercell, assigning formal charges of +4 to Ce^{4+}, and −2 to O^{2-}. In the subsequent calculations, point charges located within 3 Å of the cluster were replaced by effective core potentials [54, 55], as described in Ref.[56].

Restricted/complete active space self-consistent field (RASSCF/CASSCF) approaches [57–61] were employed to obtain the wavefunctions of different electronic states. Relativistic effects were incorporated using the second-order Douglas–Kroll–Hess (DKH2) Hamiltonian [62–65], in combination with all-electron atomic natural orbital relativistic core-correlated basis sets of valence triple-ζ quality (ANO-RCC-VTZP). The resolution-of-the-identity Cholesky decomposition technique [66] was applied to accelerate the evaluation of two-electron integrals. A finite nuclear model [67] was also employed. Transitions were then calculated using the Restricted Active Space State Interaction (RASSI) method with spin–orbit coupling (SOC) [68]. Both singlet and triplet states were included in the SOC-RASSI calculations.

The in-house program Polarixs, available as Python package [69], was used to convolute the matrix elements extracted from OpenMolcas to obtain the tensor in Eq. 29 and subsequently estimate the first and second order polarization dependent cross sections in Eq. 8. The broadening effects of Γ_n (width of the intermediate states in Eq. 29) and Γ_f (width of the final states in Eq. 8) are implemented numerically by convolution with Lorentzian functions of the corresponding widths.

The energy scale of the calculation was downshifted by 32 eV to align with the experiment.

B. Results and discussion

CeO_2 crystallizes in the $Fm\bar{3}m$ space group, with Ce ions occupying sites of O_h point symmetry. The Ce $4f$ states hybridize with O $2p$ orbitals to form a bonding state, corresponding to the ground state $|g\rangle$, and an antibonding state [70, 71]. Due to the closed-shell configuration, both the ground state $|g\rangle$ and the antibonding state are totally symmetric and thus transform according to the A_{1g} irreducible representation.

1. Core-to-core L_3M_5 RIXS

In Fig. 3 we show the ctc RIXS plane for one of the analyzers. The main features at 4840 eV emission energy correspond to the L_3M_5 resonant emission line ($2p_{3/2} \rightarrow 5d_{5/2}$), while the weaker features at 4822 eV are the L_3M_4 ($L_{\alpha 2}$) line ($2p_{3/2} \rightarrow 5d_{3/2}$). The transition paths for the L_3M_5 RIXS process are

$$|g\rangle \rightarrow |2p^5 4f^{0/1} 5d^1\rangle \rightarrow |3d^9 4f^{0/1} 5d^1\rangle$$

and were discussed in detail in Ref. [72]. Subsequently, the main features in the RIXS plane arise from E1E1 processes and can be grouped into two sets, corresponding to final-state configurations with $4f^1$ and $4f^0$ character, respectively (see annotations for L_3M_5 in Fig. 3). Within each group, the crystal-field splitting between the e_g and t_{2g} components is clearly resolved.

The constant emission energy (CEE) cuts are shown in Fig. 4. All cuts were normalized to their respective area, which is intended to compensate for non-identical reflection intensity of the analyzer crystals and partially correct for self-absorption effects that depend on the scattering angle. For both emission lines, the RIXS intensities do not exhibit a genuine dependence on the scattering angle α.

Our OpenMolcas analysis indicates the pre-edge feature originates from an E2E1 process (2p → 4f). For the L_3M_5 cuts (Fig. 4, top), the pre-edge intensity is strictly constant as a function of the scattering angle. When the absorbing atom sits on an inversion center, intraatomic p-d hybridization is symmetry forbidden and therefore

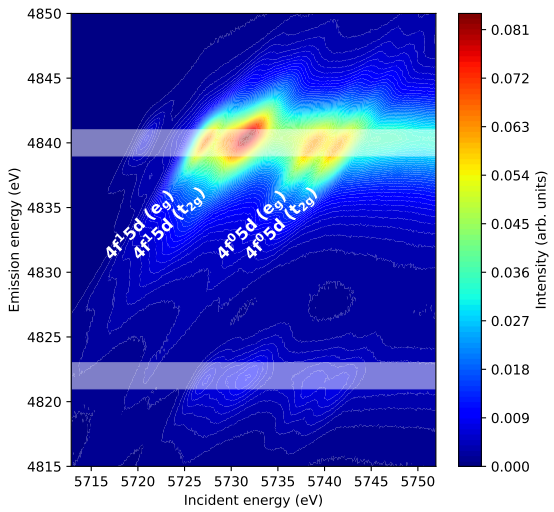

FIG. 3. Experimental $2p3d$ RIXS for the $\alpha = 118^\circ$ analyzer. Features at 4840 and 4822 eV emission energies correspond to the L_3M_5 and L_3M_4 lines respectively. Peaks are annotated according to the final state they are originating from. The displayed masks were used to obtain the CEE cuts in Fig. 4.

pre-edge peaks are essentially E2E1. For π incoming polarization, Eq. 47 predicts a pre-peak intensity independent on the scattering angle, which is consistent with the L_3M_5 experimental data. On the other hand, one can see from Fig. 3 that the pre-edge structure of L_3M_4 is affected by the tails of the E1E1 peaks above, belonging to L_3M_5. This explains why the L_3M_4 pre-edge structure is more prominent than the L_3M_5 one, and its subsequent slight angular dependence.

While the CEE cuts in Fig. 3 are consistent with the result in Eq. 47, namely that E2E1 features in π incident polarizations are independent of the scattering angle, the absence of an angular dependence in the E1E1 peaks is less immediately apparent. Although we unambiguously reproduce this behavior numerically (not shown), we further support these results with an analytical explanation. Such approach is tractable in high-symmetry situations, e.g. in O_h symmetry, but generally becomes impractical for lower-symmetry environments or for systems with higher electronic occupation numbers. The derivation is discussed in appendices A and B. For both transition paths we obtain:

$$\begin{aligned} I_{3d^95d^1_{e_g}} &= \frac{|\varepsilon_i|^2|\varepsilon_o|^2}{30} \times \frac{66+\cos^2\alpha}{45} R^2_{2p3d} \\ I_{3d^95d^1_{t_{2g}}} &= \frac{|\varepsilon_i|^2|\varepsilon_o|^2}{30} \times \frac{66+\cos^2\alpha}{30} R^2_{2p3d} \end{aligned} \quad (50)$$

These results clearly show that, even if the α dependent term is non-zero, its contribution is much weaker than the constant term and therefore the angular dependence is not seen in the experiment.

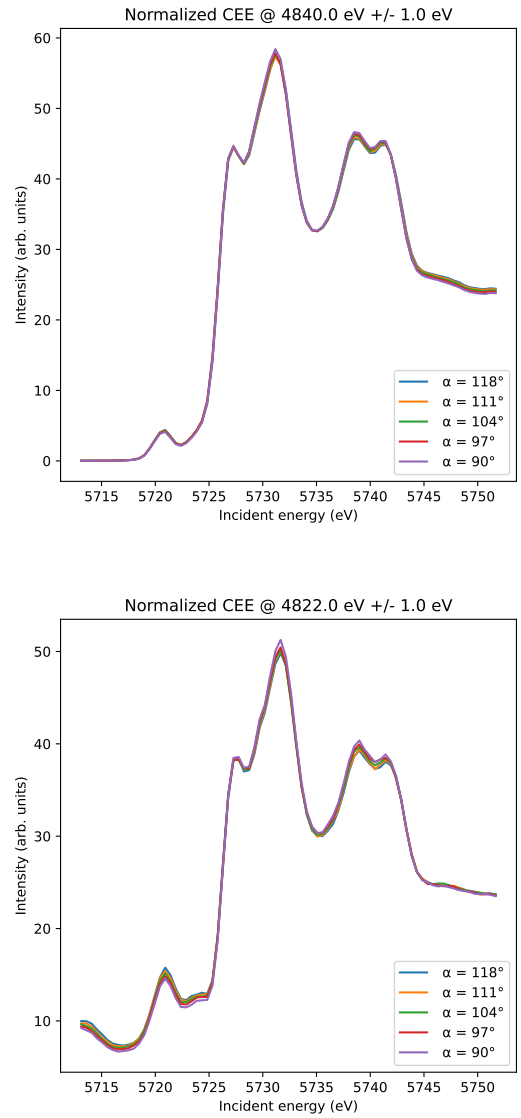

FIG. 4. CEE cuts for all analyzers obtained with the masks in Fig. 3. There is no significant angular dependence for L_3M_5 (top) and L_3M_4 RIXS (bottom).

2. *Valence-to-core RIXS*

The measured vtc RIXS planes are shown in Fig. 5. The corresponding theoretical planes were computed by convoluting the transition amplitudes obtained with OpenMolcas for the different analyzer orientations. Reasonable agreement is obtained; however, a detailed discussion is deferred to future work, as the present study focuses exclusively on the angular dependence.

The only RIXS feature exhibiting obvious angular dependence is situated at 6.5 eV energy loss (Fig. 5). The corresponding constant energy transfer (CET) cuts are shown in Fig. 6 (top). Our calculations quantitatively reproduce this result (Fig. 6, bottom).

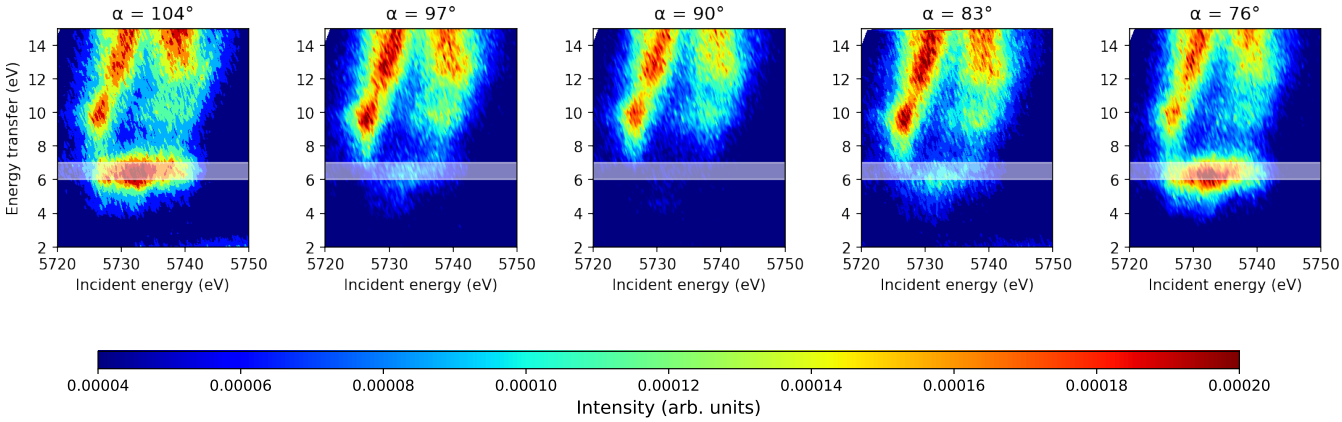

FIG. 5. Valence-to-core RIXS planes recorded for each analyzer are shown. The applied mask isolates the angular-dependent feature at an energy loss of 6.5 eV, with a bandwidth of 1 eV.

The transition path associated to this peak involves intermediate states of type $2p^5 4f^{0/1} 5d^1$, all decaying to the antibonding state. Alternatively, one can describe this process as the excitation of a $2p$ electron to a d state, followed by its decay that fills the core hole and, due to the core-hole interaction, concomitantly triggers a valence band excitation (i.e. an electron is promoted from the bonding to the antibonding state). For this pathway, the same electron is involved in both absorption and emission steps of the RIXS process. Depending on the authors, this is referred as a *participator* [72] or *indirect* RIXS process [73], in contrast to *spectator* or *direct* RIXS processes, which involve two distinct electrons.

From a group-theoretical perspective, the transition pathway associated to the 6.5 eV energy loss peak is peculiar in that it connects initial and final states of A_{1g} symmetry. In this case the scattering is isotropic (Thomson-like) with the following structure of the $\mathbf{M}$ tensor:

$$M_{A_{1g}} = \frac{1}{\sqrt{3}} \begin{bmatrix} 1 & 0 & 0 \\ 0 & 1 & 0 \\ 0 & 0 & 1 \end{bmatrix}$$

and the angular dependence:

$$I_{A_{1g}}(\alpha) = \frac{|\boldsymbol{\varepsilon}_i|^2 |\boldsymbol{\varepsilon}_o|^2}{30} \times \frac{1}{6} R^2_{A_{1g}} \cos^2 \alpha \tag{51}$$

where $R_{A_{1g}}$ is a coefficient proper to this particular final state. For this peak, the angular dependence is the most pronounced, as the tensor structure enforces a cancellation of the constant term ($a = 0$ in Eq. 38).

The angular dependence given in Eq. 51 predicts a complete suppression of the intensity for the central analyzer at $\alpha = 90°$. While this behavior is qualitatively observed in the measured RIXS planes (Fig. 5), the corresponding cut shown in Fig. 6 exhibits a small residual intensity. This background signal originates from the finite size of the analyzer crystals, on one hand, as well as from the tails of neighboring spectral features, on the other hand. The latter can be reproduced by the Polarixs calculations (see Fig. 6, bottom). We deliberately selected convolution widths ($\Gamma_n = 4$ eV for the intermediate states, $\Gamma_f = 1.5$ eV for the final states) that reveal the fine structure in the CET cuts. Increasing Γ_n would progressively smear out these features. A similar analysis establishing the lack of angular dependence of the direct RIXS peaks is provided in the Supplementary Information.

The application of our framework to vtc RIXS at the Ce L_3 edge in CeO_2 is consistent with earlier results reported by Kotani et al. [72]. They were first to accurately explain the origin of the L_3M_5 and vtc RIXS features, which are confirmed by our current study with OpenMolcas. To explain the pronounced angular dependence of participator processes—absent in spectator processes—, Kotani et al. employed simplified concepts based on a spherical-tensor decomposition (Eq. 7 of Ref. [72]), combined with the angular dependence derived in an earlier work (Eq. 2.13 of Ref. [35]). Within this framework, participator processes were argued to selectively probe a specific, angular-dependent component of the spherical tensor, whereas for spectator processes no such selection occurs, leading to a cancellation of the angular dependence. While Ref. [72] successfully accounts for the experimental observations, this early study suffers from several limitations. In particular, the scattering process is treated within an isotropic approximation, which is adequate for the 6.5 eV energy loss transition owing to the A_{1g} character of the corresponding final state, but fails to capture the tensor nature of the scattering for more general final state symmetries. From a group-theoretical perspective, the angular expression employed is incomplete and therefore cannot describe the polarization dependence in more complex situations. Specifically, an expansion up to second order would have been required in Eq. 7 of Ref. [72] to render the formulation more general; even then, its applicability would remain restricted to systems with O_h

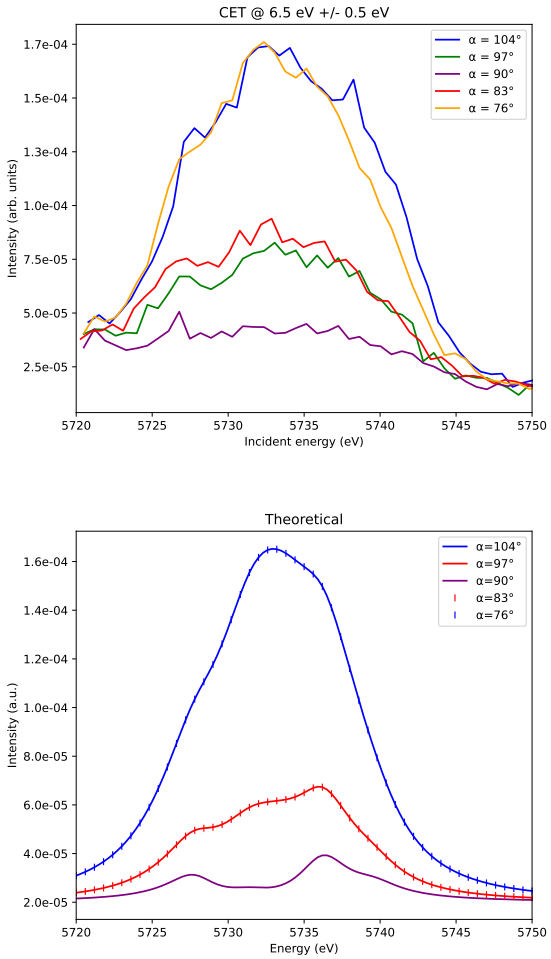

FIG. 6. Angular dependence in vtc RIXS. Top: constant energy transfer cuts in the measured vtc RIXS planes with the mask displayed in Fig. 5. Those analyzers disposed symmetrically wrt. 90° have similar signals. Bottom: angular dependence predicted from calculations. The signals with $\alpha = 90° + \Delta\alpha$ and $\alpha = 90° - \Delta\alpha$ are strictly identical.

symmetry.

V. CONCLUSION

This work presents a practical approach to interpreting angular and polarization dependent XAS and RIXS spectra in orientation-averaged systems, such as liquid or powder samples. By working directly with Cartesian transition tensors—the natural output of modern quantum chemistry codes—our approach bypasses the complexity of spherical tensor formalisms while maintaining full generality and rigor.

The key advantages of this framework are threefold. First, it provides explicit, closed-form expressions for orientation-averaged intensities that cleanly separate experimental geometry from sample electronic structure, enabling straightforward interpretation of polarization-dependent measurements. Second, it handles arbitrary point-group symmetries without requiring case-by-case derivations, making it broadly applicable across diverse materials systems. Third, it seamlessly integrates with ab initio calculations from packages like OpenMolcas and ORCA, eliminating the need for coordinate transformations and enabling quantitative predictions of spectral features.

We present the first derivation of RIXS powder averages within a Cartesian tensor framework, providing explicit formulae for the E1E1, E1E2, and E2E1 contributions, together with a systematic methodology for obtaining the E2E2 term and even higher order terms.

We validated our approach through detailed analysis of RIXS measurements at the Ce L_3 edge in CeO_2. The framework successfully reproduces the absence of angular dependence in L_3M_5 RIXS and explains the pronounced $\cos^2\alpha$ behavior of the 6.5 eV vtc feature — arising from its unique totally symmetric A_{1g} final state, combined to the closed shell electronic structure of the ground state. For verification and educational purposes, group theory was employed to deduce the analytical angular dependence for each transition.

Our formalism naturally treats circular polarization for electric multipole transitions (E1 and E2) and reproduces the known result that E1E2 interference in absorption vanishes upon orientational averaging.

While the current formulation addresses non-magnetic and non-chiral systems, the theoretical framework introduced in this work is already capable of addressing certain cases beyond these limits, such as magnetic scattering without additional transition operators and single-handed chiral structures (since Eq. 12 assumes the crystal is generated by real operators). The tensor-based foundation naturally extends to more complex scenarios. Future work incorporating complete magnetic and chiral contributions will require higher-rank tensors, but the Cartesian framework established here provides a clear pathway forward. More generally, this methodology applies to a wide range of X-ray spectroscopies—including non-resonant X-ray Raman scattering—as well as to optical spectroscopies such as Raman and UV–Vis. It can be straightforwardly extended to higher-order multipole processes (E2E2, E3E1, etc.) within the same systematic framework.

ACKNOWLEDGMENTS

We thank Blanka Detlefs for help with the data acquisition and processing and Vasyl Marchuk for preparing the sample. One of the authors (O. Bunău) thanks Yves Joly and Andrei Rogalev for fruitful discussions. This work was co-financed by the European Union through an Erasmus Mundus grant from the Education, Audiovisual, and Culture Executive Agency (EACEA).

Appendix A: Polarization dependence of different irreducible representations under O_h symmetry

A symmetry analysis of the tensor elements defined in Eq. 29 shows that when the ground state $|g\rangle$ belongs to A_{1g}, both the E1E1 scattering tensor and the accessible final states $|f\rangle$ transform according to the direct product

$$T_{1u} \otimes T_{1u} = A_{1g} \oplus E_g \oplus T_{1g} \oplus T_{2g} \tag{A1}$$

In particular, the **M** tensor structure is fully defined by the irreducible representation (irrep) the corresponding final state belongs to.

Every peak in the RIXS plane generally contains the summed contributions from various final states. Because the summation over final states appears outside the modulus squared in Eq. 8, final states do not mix with each other. Therefore, the polarization dependence must be analyzed separately for each final state and then summed up together. Depending on the decomposition of the final state, not all irreps are necessarily present in the sum, or they may be represented more than once.

This section gives (a) the angular dependence of each irrep (for simplicity, as π-incident without polarization detection) and (b) the basis matrices for the **M** tensor description.

If the final state is A_{1g}, the transition tensor is isotropic and described by the diagonal matrix:

$$\frac{1}{\sqrt{3}}\begin{bmatrix}1 & 0 & 0\\ 0 & 1 & 0\\ 0 & 0 & 1\end{bmatrix}$$

and the angular dependence:

$$I_{A_{1g}} = \frac{|\boldsymbol{\varepsilon}_i|^2|\boldsymbol{\varepsilon}_o|^2}{30} \times \frac{1}{6} R^2_{A_{1g}} \cos^2\alpha \tag{A2}$$

Here, $R_{A_{1g}}$ is a coefficient depending on the final state and its irrep.

The transition to the E_g irrep spans a twofold-degenerate subspace, for which two commonly used basis tensors are

$$\frac{1}{\sqrt{2}}\begin{bmatrix}1 & 0 & 0\\ 0 & -1 & 0\\ 0 & 0 & 0\end{bmatrix} \quad \text{and} \quad \frac{1}{\sqrt{6}}\begin{bmatrix}-1 & 0 & 0\\ 0 & -1 & 0\\ 0 & 0 & 2\end{bmatrix}$$

A noteworthy property of the E_g representation is that any choice of basis within this subspace, leads to the same polarization dependence, namely:

$$I_{E_g} = \frac{|\boldsymbol{\varepsilon}_i|^2|\boldsymbol{\varepsilon}_o|^2}{30} \times \frac{1}{10} R^2_{E_g}\left(1 + \frac{1}{6}\cos^2\alpha\right) \tag{A3}$$

Similarly, T_{2g} is three-fold degenerate and can only give off-symmetric diagonal matrices like:

$$\frac{1}{\sqrt{2}}\begin{bmatrix}0 & 0 & 0\\ 0 & 0 & 1\\ 0 & 1 & 0\end{bmatrix} \text{ and } \frac{1}{\sqrt{2}}\begin{bmatrix}0 & 0 & 1\\ 0 & 0 & 0\\ 1 & 0 & 0\end{bmatrix} \text{ and } \frac{1}{\sqrt{2}}\begin{bmatrix}0 & 1 & 0\\ 1 & 0 & 0\\ 0 & 0 & 0\end{bmatrix}$$

yielding a similar dependence (up to a factor) to E_g:

$$I_{T_{2g}} = \frac{|\boldsymbol{\varepsilon}_i|^2|\boldsymbol{\varepsilon}_o|^2}{30} \times \frac{1}{10} R^2_{T_{2g}}\left(1 + \frac{1}{6}\cos^2\alpha\right) \tag{A4}$$

T_{1g} is described by off anti-symmetric diagonal matrices of type:

$$\frac{1}{\sqrt{2}}\begin{bmatrix}0 & 0 & 0\\ 0 & 0 & 1\\ 0 & -1 & 0\end{bmatrix} \text{ and } \frac{1}{\sqrt{2}}\begin{bmatrix}0 & 0 & 1\\ 0 & 0 & 0\\ -1 & 0 & 0\end{bmatrix} \text{ and } \frac{1}{\sqrt{2}}\begin{bmatrix}0 & 1 & 0\\ -1 & 0 & 0\\ 0 & 0 & 0\end{bmatrix}$$

with subsequently:

$$I_{T_{1g}} = \frac{|\boldsymbol{\varepsilon}_i|^2|\boldsymbol{\varepsilon}_o|^2}{30} \times \frac{1}{6} R^2_{T_{1g}}\left(1 - \frac{1}{2}\cos^2\alpha\right) \tag{A5}$$

Note that for T_{1g} and T_{2g} representations, contrary to E_g, rotations of the standard basis will not lead to the same angular dependence.

The total intensity is the sum of all contributing final states, each described within an irrep and weighted by their respective dimensions:

$$I \;=\; I_{A_{1g}} + 2I_{E_g} + 3I_{T_{1g}} + 3I_{T_{2g}} \tag{A6}$$

The exact relationship between the various state coefficients ($R_{A_{1g}}$, $R_{T_{2g}}$, R_{E_g}, $R_{T_{1g}}$) depends on the specific final state and their approximated calculation is explicated in appendix B.

Appendix B: O_h spin-free $2p3d$ E1E1 transition polarization dependence

This section gives the angular dependence of various final configurations involved in the L_3M_5 RIXS, i.e. $3d^9 5d^1_{e_g}$ and $3d^9 5d^1_{t_{2g}}$, both composed from several final states.

Based on the decomposed tensor structure, it is possible to figure out the relation among factors R under different irreps. The transition follows the configuration change $|g\rangle \to |2p^5 4f^{0/1} 5d^1\rangle \to |3d^9 4f^{0/1} 5d^1\rangle$. The transition tensor structure is totally determined by the electron configuration of $3d^9 5d^1$. The configuration $4f^{0/1}$ doesn't affect the irreps, because for $4f^1$ case, an additional electron-hole pair locates at two a_{2u} (f-like) orbitals, as compared to $4f^0$. Given $a_{2u} \times a_{2u} = A_{1g}$, this additional pair doesn't change the irrep of $3d^9 5d^1$ configuration.

We define the integral:

$$|\,\langle 2p_x|\, x\, |5d_{x^2-y^2}\rangle\, \langle 3d_{xy}|\, y\, |2p_x\rangle\,| = R_{2p3d} \tag{B1}$$

for a particular choice of the polarization directions. All transition tensors can be scaled to R_{2p3d}. Assuming the excited electron locates at $5d_{x^2-y^2}$ and considering all intermediate states ($2p_x$, $2p_y$ and $2p_z$), the corresponding

transition amplitude (for the same choice of polarization) is:

$$\mathbf{D}_{gn} = |\langle 2p_x| x |5d_{x^2-y^2}\rangle| \begin{bmatrix} 1 & 0 & 0 \\ 0 & -1 & 0 \\ 0 & 0 & 0 \end{bmatrix} \begin{bmatrix} |2p_x\rangle \\ |2p_y\rangle \\ |2p_z\rangle \end{bmatrix} \tag{B2}$$

and similarly, assuming the final state hole is $3d_{xy}$, the corresponding transition amplitude:

$$\mathbf{D}_{nf} = |\langle 3d_{xy}| y |2p_x\rangle| \begin{bmatrix} 0 & 1 & 0 \\ 1 & 0 & 0 \\ 0 & 0 & 0 \end{bmatrix} \begin{bmatrix} |2p_x\rangle \\ |2p_y\rangle \\ |2p_z\rangle \end{bmatrix} \tag{B3}$$

The E1E1 transition to the final state $3d_{xy}5d^1_{x^2-y^2}$ is (similar to $3d^9$ with hole in xy):

$$\mathbf{M} = \mathbf{D}_{gn} \otimes \mathbf{D}_{nf} = R_{2p3d} \begin{bmatrix} 0 & 1 & 0 \\ -1 & 0 & 0 \\ 0 & 0 & 0 \end{bmatrix} \tag{B4}$$

a general result regardless of the polarization directions. All tensors can be calculated in the same approach.

The $3d$ orbitals in O_h belong to either e_g or t_{2g} and therefore the final states with the structure $3d^9 5d^1$ decompose to:

$$\begin{aligned} 3d^9 5d^1_{e_g}: &\ (e_g \oplus t_{2g}) \otimes e_g = (e_g \otimes e_g) \oplus (e_g \otimes t_{2g}) \\ 3d^9 5d^1_{t_{2g}}: &\ (e_g \oplus t_{2g}) \otimes t_{2g} = (t_{2g} \otimes t_{2g}) \oplus (e_g \otimes t_{2g}) \end{aligned} \tag{B5}$$

Based on this, we calculate all transition tensors $\mathbf{N}$ between the different subspaces in Eq. B5.

$e_g \otimes e_g$	$d_{x^2-y^2}$	d_{z^2}
$d_{x^2-y^2}$	$\begin{bmatrix} 1 & 0 & 0 \\ 0 & 1 & 0 \\ 0 & 0 & 0 \end{bmatrix}$	$\begin{bmatrix} -\frac{1}{\sqrt{3}} & 0 & 0 \\ 0 & \frac{1}{\sqrt{3}} & 0 \\ 0 & 0 & 0 \end{bmatrix}$
d_{z^2}	$\begin{bmatrix} -\frac{1}{\sqrt{3}} & 0 & 0 \\ 0 & \frac{1}{\sqrt{3}} & 0 \\ 0 & 0 & 0 \end{bmatrix}$	$\begin{bmatrix} \frac{1}{3} & 0 & 0 \\ 0 & \frac{1}{3} & 0 \\ 0 & 0 & \frac{4}{3} \end{bmatrix}$

(B6)

$e_g \otimes t_{2g}$	$d_{x^2-y^2}$	d_{z^2}
d_{xy}	$\begin{bmatrix} 0 & 1 & 0 \\ -1 & 0 & 0 \\ 0 & 0 & 0 \end{bmatrix}$	$\begin{bmatrix} 0 & -\frac{1}{\sqrt{3}} & 0 \\ -\frac{1}{\sqrt{3}} & 0 & 0 \\ 0 & 0 & 0 \end{bmatrix}$
d_{yz}	$\begin{bmatrix} 0 & 0 & 0 \\ 0 & 0 & -1 \\ 0 & 0 & 0 \end{bmatrix}$	$\begin{bmatrix} 0 & 0 & 0 \\ 0 & 0 & \frac{2}{\sqrt{3}} \\ 0 & -\frac{1}{\sqrt{3}} & 0 \end{bmatrix}$
d_{xz}	$\begin{bmatrix} 0 & 0 & 1 \\ 0 & 0 & 0 \\ 0 & 0 & 0 \end{bmatrix}$	$\begin{bmatrix} 0 & 0 & \frac{2}{\sqrt{3}} \\ 0 & 0 & 0 \\ -\frac{1}{\sqrt{3}} & 0 & 0 \end{bmatrix}$

(B7)

$t_{2g} \otimes t_{2g}$	d_{xy}	d_{yz}	d_{xz}
d_{xy}	$\begin{bmatrix} 1 & 0 & 0 \\ 0 & 1 & 0 \\ 0 & 0 & 0 \end{bmatrix}$	$\begin{bmatrix} 0 & 0 & 1 \\ 0 & 0 & 0 \\ 0 & 0 & 0 \end{bmatrix}$	$\begin{bmatrix} 0 & 0 & 0 \\ 0 & 0 & 1 \\ 0 & 0 & 0 \end{bmatrix}$
d_{yz}	$\begin{bmatrix} 0 & 0 & 0 \\ 0 & 0 & 0 \\ 1 & 0 & 0 \end{bmatrix}$	$\begin{bmatrix} 0 & 0 & 0 \\ 0 & 1 & 0 \\ 0 & 0 & 1 \end{bmatrix}$	$\begin{bmatrix} 0 & 0 & 0 \\ 1 & 0 & 0 \\ 0 & 0 & 0 \end{bmatrix}$
d_{xz}	$\begin{bmatrix} 0 & 0 & 0 \\ 0 & 0 & 0 \\ 0 & 1 & 0 \end{bmatrix}$	$\begin{bmatrix} 0 & 1 & 0 \\ 0 & 0 & 0 \\ 0 & 0 & 0 \end{bmatrix}$	$\begin{bmatrix} 1 & 0 & 0 \\ 0 & 0 & 0 \\ 0 & 0 & 1 \end{bmatrix}$

(B8)

The matrices of the irreps product form a new space. To get the final state structure, we need to decompose these spaces into subspaces represented by irreps. The irrep subspace can be calculated by projection. The Hilbert-Schmidt inner production of $\mathbf{N}$ on a base $\mathbf{B}$ is defined as following:

$$P_{\mathbf{B}} = \mathrm{Tr}(\mathbf{N}^* \mathbf{B}) \tag{B9}$$

where the bases $\mathbf{B}$ have already been shown in appendix A.

In the following we calculate the scaling coefficients R/R_{2p3d}, for each subspace.

$e_g \otimes e_g = A_{1g} \oplus A_{2g} \oplus E_g$:

$A_{1g} \subset e_g \otimes e_g$	$d_{x^2-y^2}$	d_{z^2}
$d_{x^2-y^2}$	$\frac{2}{\sqrt{3}}$	0
d_{z^2}	0	$\frac{2}{\sqrt{3}}$

(B10)

$$\begin{aligned} R^{e_g \otimes e_g}_{A_{1g}}/R_{2p3d} &= \sqrt{\left(\frac{2}{\sqrt{3}}\right)^2 + \left(\frac{2}{\sqrt{3}}\right)^2} \\ &= 2\sqrt{\frac{2}{3}} \end{aligned} \tag{B11}$$

For components with dimension larger than 1, e.g. E_g, we get the same coefficient values for any of the basis matrices $\mathbf{B}$, as is shown below:

$E_g \subset e_g \otimes e_g$	$d_{x^2-y^2}$	d_{z^2}
$d_{x^2-y^2}$	$0, -\sqrt{\frac{2}{3}}$	$-\sqrt{\frac{2}{3}}, 0$
d_{z^2}	$-\sqrt{\frac{2}{3}}, 0$	$0, \sqrt{\frac{2}{3}}$

(B12)

$$\begin{aligned} R^{e_g \otimes e_g}_{E_g}/R_{2p3d} &= \sqrt{\left(-\sqrt{\frac{2}{3}}\right)^2 + \left(-\sqrt{\frac{2}{3}}\right)^2} \\ &= \sqrt{\left(-\sqrt{\frac{2}{3}}\right)^2 + \left(\sqrt{\frac{2}{3}}\right)^2} \\ &= \frac{2}{\sqrt{3}} \end{aligned} \tag{B13}$$

Since A_{2g} is not an allowed final state symmetry by E1E1 transition, we do not further treat it here.

$e_g \otimes t_{2g} = T_{1g} \oplus T_{2g}$:

$T_{1g} \subset e_g \otimes t_{2g}$	$d_{x^2-y^2}$	d_{z^2}
d_{xy}	$0, 0, \sqrt{2}$	$0, 0, 0$
d_{yz}	$0, \frac{1}{\sqrt{2}}, 0$	$0, -\sqrt{\frac{3}{2}}, 0$
d_{xz}	$-\frac{1}{\sqrt{2}}, 0, 0$	$-\sqrt{\frac{3}{2}}, 0, 0$

(B14)

$$\begin{aligned} R^{e_g\otimes t_{2g}}_{T_{1g}}/R_{2p3d} &= \sqrt{(\sqrt{2})^2} \\ &= \sqrt{\left(\frac{1}{\sqrt{2}}\right)^2 + \left(-\sqrt{\frac{3}{2}}\right)^2} \\ &= \sqrt{\left(-\frac{1}{\sqrt{2}}\right)^2 + \left(-\sqrt{\frac{3}{2}}\right)^2} \\ &= \sqrt{2} \end{aligned} \tag{B15}$$

$T_{2g} \subset e_g \otimes t_{2g}$	$d_{x^2-y^2}$	d_{z^2}
d_{xy}	$0, 0, 0$	$0, 0, -\sqrt{\frac{2}{3}}$
d_{yz}	$0, -\frac{1}{\sqrt{2}}, 0$	$0, \frac{1}{\sqrt{6}}, 0$
d_{xz}	$\frac{1}{\sqrt{2}}, 0, 0$	$-\frac{1}{\sqrt{6}}, 0, 0$

(B16)

$$\begin{aligned} R^{e_g\otimes t_{2g}}_{T_{2g}}/R_{2p3d} &= \sqrt{\left(-\sqrt{\frac{2}{3}}\right)^2} \\ &= \sqrt{\left(-\frac{1}{\sqrt{2}}\right)^2 + \left(\frac{1}{\sqrt{6}}\right)^2} \\ &= \sqrt{\left(\frac{1}{\sqrt{2}}\right)^2 + \left(-\frac{1}{\sqrt{6}}\right)^2} \\ &= \sqrt{\frac{2}{3}} \end{aligned} \tag{B17}$$

$t_{2g} \otimes t_{2g} = A_{1g} \oplus E_g \oplus T_{1g} \oplus T_{2g}$:

$A_{1g} \subset t_{2g} \otimes t_{2g}$	d_{xy}	d_{yz}	d_{xz}
d_{xy}	$\frac{2}{\sqrt{3}}$	0	0
d_{yz}	0	$\frac{2}{\sqrt{3}}$	0
d_{xz}	0	0	$\frac{2}{\sqrt{3}}$

(B18)

$$\begin{aligned} R^{t_{2g}\otimes t_{2g}}_{A_{1g}}/R_{2p3d} &= \sqrt{\left(\frac{2}{\sqrt{3}}\right)^2 + \left(\frac{2}{\sqrt{3}}\right)^2 + \left(\frac{2}{\sqrt{3}}\right)^2} \\ &= 2 \end{aligned} \tag{B19}$$

$E_g \subset t_{2g} \otimes t_{2g}$	d_{xy}	d_{yz}	d_{xz}
d_{xy}	$0, -\sqrt{\frac{2}{3}}$	$0, 0$	$0, 0$
d_{yz}	$0, 0$	$-\frac{1}{\sqrt{2}}, \frac{1}{\sqrt{6}}$	$0, 0$
d_{xz}	$0, 0$	$0, 0$	$\frac{1}{\sqrt{2}}, \frac{1}{\sqrt{6}}$

(B20)

$$\begin{aligned} R^{t_{2g}\otimes t_{2g}}_{E_g}/R_{2p3d} &= \sqrt{\left(\frac{1}{\sqrt{2}}\right)^2 + \left(\frac{1}{\sqrt{2}}\right)^2} \\ &= \sqrt{\left(-\sqrt{\frac{2}{3}}\right)^2 + \left(\frac{1}{\sqrt{6}}\right)^2 + \left(\frac{1}{\sqrt{6}}\right)^2} \\ &= 1 \end{aligned} \tag{B21}$$

$T_{1g} \subset t_{2g} \otimes t_{2g}$	d_{xy}	d_{yz}	d_{xz}
d_{xy}	$0, 0, 0$	$0, -\frac{1}{\sqrt{2}}, 0$	$-\frac{1}{\sqrt{2}}, 0, 0$
d_{yz}	$0, \frac{1}{\sqrt{2}}, 0$	$0, 0, 0$	$0, 0, \frac{1}{\sqrt{2}}$
d_{xz}	$\frac{1}{\sqrt{2}}, 0, 0$	$0, 0, -\frac{1}{\sqrt{2}}$	$0, 0, 0$

(B22)

$$\begin{aligned} R^{t_{2g}\otimes t_{2g}}_{T_{1g}}/R_{2p3d} &= \sqrt{\left(\frac{1}{\sqrt{2}}\right)^2 + \left(-\frac{1}{\sqrt{2}}\right)^2} \\ &= \sqrt{\left(\frac{1}{\sqrt{2}}\right)^2 + \left(-\frac{1}{\sqrt{2}}\right)^2} \\ &= \sqrt{\left(\frac{1}{\sqrt{2}}\right)^2 + \left(-\frac{1}{\sqrt{2}}\right)^2} \\ &= 1 \end{aligned} \tag{B23}$$

$T_{2g} \subset t_{2g} \otimes t_{2g}$	d_{xy}	d_{yz}	d_{xz}
d_{xy}	$0, 0, 0$	$0, \frac{1}{\sqrt{2}}, 0$	$\frac{1}{\sqrt{2}}, 0, 0$
d_{yz}	$0, \frac{1}{\sqrt{2}}, 0$	$0, 0, 0$	$0, 0, \frac{1}{\sqrt{2}}$
d_{xz}	$\frac{1}{\sqrt{2}}, 0, 0$	$0, 0, \frac{1}{\sqrt{2}}$	$0, 0, 0$

(B24)

$$\begin{aligned} R^{t_{2g}\otimes t_{2g}}_{T_{2g}}/R_{2p3d} &= \sqrt{\left(\frac{1}{\sqrt{2}}\right)^2 + \left(\frac{1}{\sqrt{2}}\right)^2} \\ &= \sqrt{\left(\frac{1}{\sqrt{2}}\right)^2 + \left(\frac{1}{\sqrt{2}}\right)^2} \\ &= \sqrt{\left(\frac{1}{\sqrt{2}}\right)^2 + \left(\frac{1}{\sqrt{2}}\right)^2} \\ &= 1 \end{aligned} \tag{B25}$$

The total intensity is therefore obtained by summing up the individual contributions of all irreps participating in the decomposition, weighted by their respective

dimensions. Furthermore the individual terms need to be scaled, depending on the subspace the irrep originates from. For instance, $3d^9 5d^1_{e_g}$ has $T_{2g} \oplus T_{1g}$ from $t_{2g} \otimes e_g$ and $A_{1g} \oplus E_g$ from $e_g \otimes e_g$, we therefore need to consider the angular dependencies in appendix A with the specific coefficients $R^{t_{2g}\otimes e_g}_{T_{1g}}, R^{t_{2g}\otimes e_g}_{T_{2g}}, R^{e_g\otimes e_g}_{A_{1g}}, R^{e_g\otimes e_g}_{E_g}$. After substitution:

$$\begin{aligned} I_{3d^9 5d^1_{e_g}} &= I_{A_{1g}} + 2I_{E_g} + 3I_{T_{1g}} + 3I_{T_{2g}} \\ &= \frac{|\boldsymbol{\varepsilon}_i|^2|\boldsymbol{\varepsilon}_o|^2}{30} \times \frac{66+\cos^2\alpha}{45} R^2_{2p3d} \end{aligned} \quad \text{(B26)}$$

For $3d^9 5d^1_{t_{2g}}$ we need to consider it contains T_{2g} and T_{1g} originating from both subspaces, therefore scaled distinctly. Finally:

$$I_{3d^9 5d^1_{t_{2g}}} = \frac{|\boldsymbol{\varepsilon}_i|^2|\boldsymbol{\varepsilon}_o|^2}{30} \times \frac{66+\cos^2\alpha}{30} R^2_{2p3d} \quad \text{(B27)}$$

The spin-free vtc E1E1 transition polarization dependence can be deduced in a similar way.

In conclusion, we need to justify why including spin-orbit coupling (SOC) does not significantly alter the polarization dependencies derived in appendices A and B. For the considered transitions, each shell contains at most one electron or one hole. When SOC is included, each irrep splits into several related final states, contributing to different edges. SOC acts as a perturbation, causing only minor quantitative changes, primarily affecting the overall magnitude of the dependence rather than the relative weights of the irreps. Therefore, the polarization dependence remains qualitatively similar to the spin-free (SF) case even when SOC is included.

Appendix C: Comparison between theory and *ab initio* calculations

This section compares the L_3M_5 RIXS irreps coefficients ratio from the group theory (analytical) to the *ab initio* numerical results in OpenMolcas.

TABLE II. Intensity ratio of SF and SOC ($L_{\alpha 1}$) for the $5d_{e_g}$ peaks.

Ratio	Theory	$\lvert 3d^9 4f^1 5d^1_{e_g}\rangle$		$\lvert 3d^9 4f^0 5d^1_{e_g}\rangle$	
		SF	SOC	SF	SOC
$R^2_{A_{1g}}/R^2_{T_{2g}}$	4	3.63	3.76	3.61	3.62
$R^2_{E_g}/R^2_{T_{2g}}$	2	1.99	1.99	2.00	2.00
$R^2_{T_{1g}}/R^2_{T_{2g}}$	3	3.02	3.01	3.04	3.00

The expected values for the $|3d^9 4f^{0/1} 5d^1\rangle$ configurations are reported in Tabs. II and III. When a single irrep contains more than one final state, their squared contributions sum up. We conclude that the theoretical (analytical) results are consistent with the numerical ones for both configurations. Owing to the rotational properties of the E_g basis, the SOC states of the $5d^1_{e_g}$ configuration exhibit an angular dependence that is only slightly modified with respect to the SF case presented in Appendix A. This is no longer the case for the $5d^1_{t_{2g}}$ configuration, where the coupling among different components within the t_{2g} irrep leads to a substantial modification of the angular dependence of the individual irreps. Nevertheless, the calculations show that the *total* intensity, i.e., after summing over all relevant irreps, does not change significantly between the SF and SOC scenarios.

TABLE III. Intensity ratio of SF $5d_{t_{2g}}$ peaks.

Ratio	Theory	$\lvert 3d^9 4f^1 5d^1_{t_{2g}}\rangle$	$\lvert 3d^9 4f^0 5d^1_{t_{2g}}\rangle$
$R^2_{A_{1g}}/R^2_{E_g}$	4	4.00	4.04
$R^2_{T_{1g}}/R^2_{E_g}$	3	2.96	3.06
$R^2_{T_{2g}}/R^2_{E_g}$	1.67	1.65	1.62

Appendix D: Equivalence to the spherical tensor method

In this work, the XAS intensity expressions are given in Eq. 20 and Eq. 23. Equivalent formulae are explicitly presented in Ref. [46], so no further derivation is required here. We instead demonstrate that the spherical-tensor approach developed in Ref. [37] is fully equivalent to the Cartesian-tensor formulation used to perform the orientational average of E1E1 RIXS.

The spherical-tensor treatment starts from the standard SO(3) decomposition of the inner product between the transition operator $\mathbf{M}$ and its complex conjugate. Following Ref. [37], this decomposition yields three independent scalar coefficients, denoted S_0, S_1 and S_2:

$$S_b = \sum_{imjn} X_{im,jn}(b) \times M_{im} M^*_{jn} \quad \text{(D1)}$$

where

$$\begin{aligned} X_{im,jn}(b) &= \sum_{\beta=-b}^{b} (-1)^{b-\beta} \sum_{\mu\nu\mu'\nu'} \langle 1\mu' 1\nu | b\beta\rangle \langle 1\mu 1\nu' | b\bar{\beta}\rangle \\ &\quad \times A_{i\mu'} A_{m\nu} A_{n\mu} A_{j\nu'} \end{aligned} \quad \text{(D2)}$$

The A_{ij} is the transfer matrix element (projector) between Cartesian and spherical tensor ($\mu, \nu, \mu', \nu' = -1, 0, +1$):

$$\mathbf{A} = \begin{bmatrix} \frac{1}{\sqrt{2}} & 0 & -\frac{1}{\sqrt{2}} \\ \frac{i}{\sqrt{2}} & 0 & \frac{i}{\sqrt{2}} \\ 0 & 1 & 0 \end{bmatrix} \quad \text{(D3)}$$

This decomposition gives rise to the following equations:

$$\begin{aligned} S_0 &= \frac{1}{3}|\operatorname{Tr}(\mathbf{M})|^2 \\ S_1 &= \frac{1}{2}(-\operatorname{Tr}(\mathbf{M}^\dagger\mathbf{M}) + \operatorname{Tr}(\mathbf{M}^*\mathbf{M})) \\ S_2 &= \frac{1}{2}(\operatorname{Tr}(\mathbf{M}^\dagger\mathbf{M}) + \operatorname{Tr}(\mathbf{M}^*\mathbf{M})) - \frac{1}{3}|\operatorname{Tr}(\mathbf{M})|^2 \end{aligned} \tag{D4}$$

These three terms are separately the isotropic invariant, antisymmetric invariant and symmetric traceless invariant. The relationship between these invariants and intensity is given by Ref. [36]:

$$\begin{aligned} \sigma_{\mathrm{RIXS}}^{\mathrm{E1E1}} &= \sum_{g=0}^{2} S_g \cdot \left[\frac{(-1)^g}{9} - \begin{Bmatrix} 1 & 1 & g \\ 1 & 1 & 1 \end{Bmatrix} \frac{|\hat{\boldsymbol{\varepsilon}}_i \cdot \hat{\boldsymbol{\varepsilon}}_o^*|^2 - |\hat{\boldsymbol{\varepsilon}}_i \cdot \hat{\boldsymbol{\varepsilon}}_o|^2}{2} \right. \\ &+ \left. \frac{4}{(2-g)!(3+g)!} \left(\frac{|\hat{\boldsymbol{\varepsilon}}_i \cdot \hat{\boldsymbol{\varepsilon}}_o^*|^2 + |\hat{\boldsymbol{\varepsilon}}_i \cdot \hat{\boldsymbol{\varepsilon}}_o|^2}{2} - \frac{1}{3} \right) \right] \end{aligned}$$

After reduction, the final intensity formula is:

$$\begin{aligned} \sigma_{\mathrm{RIXS}}^{\mathrm{E1E1}} &= -\frac{S_1}{6} + \frac{S_2}{10} + \left(\frac{S_0}{3} - \frac{S_2}{15} \right) |\hat{\boldsymbol{\varepsilon}}_i \cdot \hat{\boldsymbol{\varepsilon}}_o^*|^2 \\ &+ \left(\frac{S_1}{6} + \frac{S_2}{10} \right) |\hat{\boldsymbol{\varepsilon}}_i \cdot \hat{\boldsymbol{\varepsilon}}_o|^2 \end{aligned} \tag{D5}$$

After putting Eq. D4 into Eq. D5, the intensity formula become identical to the Eq. 32 obtained within our formalism.

[1] M. Abu-Samak, U. Kumar, A. Quraishi, R. Kumar, S. Kumar, S. Dalela, M. A. Ahmad, B. Choudhary, and P. Alvi, Physica B **628**, 413562 (2022).
[2] F. M. F. de Groot, M. W. Haverkort, H. Elnaggar, A. Juhin, K.-J. Zhou, and P. Glatzel, Nat. Rev. Methods Primers **4**, 45 (2024).
[3] P. Glatzel and U. Bergmann, Coord. Chem. Rev. **249**, 65 (2005).
[4] M. Guo, O. Prakash, H. Fan, L. H. M. de Groot, V. F. Hlynsson, S. Kaufhold, O. Gordivska, N. Velásquez, P. Chabera, P. Glatzel, K. Wärnmark, P. Persson, and J. Uhlig, Phys. Chem. Chem. Phys. **22**, 9067 (2020).
[5] H. Y. Huang, A. Singh, C. I. Wu, J. D. Xie, J. Okamoto, A. A. Belik, E. Kurmaev, A. Fujimori, C. T. Chen, S. V. Streltsov, and D. J. Huang, npj Quantum Mater. **7**, 33 (2022).
[6] H. A. S. Orduz, L. Bugarin, S.-L. Heck, P. Dolcet, M. Casapu, J.-D. Grunwaldt, and P. Glatzel, J. Synchrotron Radiat. **31**, 733 (2024).
[7] A. Svyazhin, V. Nalbandyan, M. Rovezzi, A. Chumakova, B. Detlefs, A. A. Guda, A. Santambrogio, A. Manceau, and P. Glatzel, Inorg. Chem. **61**, 869 (2022).
[8] A. Beheshti Askari, M. al Samarai, N. Hiraoka, H. Ishii, L. Tillmann, M. Muhler, and S. DeBeer, Nanoscale **12**, 15185 (2020).
[9] M. L. Traulsen, H. W. P. de Carvalho, P. Zielke, and J. D. Grunwaldt, J. Electrochem. Soc. **164**, F3064 (2017).
[10] A. Pedersen, K. Kumar, Y.-P. Ku, V. Martin, L. Dubau, K. T. Santos, J. Barrio, V. A. Saveleva, P. Glatzel, V. K. Paidi, X. Li, A. Hutzler, M.-M. Titirici, A. Bonnefont, S. Cherevko, I. E. L. Stephens, and F. Maillard, Energy Environ. Sci. **17**, 6323 (2024).
[11] A. Longo, F. Giannici, M. P. Casaletto, M. Rovezzi, C. J. Sahle, P. Glatzel, Y. Joly, and A. Martorana, ACS Catal. **12**, 3615 (2022).
[12] P. Zasimov, L. Amidani, M. Retegan, O. Walter, R. Caciuffo, and K. O. Kvashnina, Inorg. Chem. **61**, 1817 (2022).
[13] S. M. Butorin, K. O. Kvashnina, J. R. Vegelius, D. Meyer, and D. K. Shuh, Proc. Natl. Acad. Sci. U.S.A. **113**, 8093 (2016).
[14] L. Amidani, J. J. Joos, P. Glatzel, and J. c. v. Kolorenč, Phys. Rev. Lett. **134**, 046401 (2025).
[15] T. G. Burrow, N. M. Alcock, M. S. Huzan, M. A. Dunstan, J. A. Seed, B. Detlefs, P. Glatzel, M. O. J. Y. Hunault, J. Bendix, K. S. Pedersen, and M. L. Baker, J. Am. Chem. Soc. **146**, 22570 (2024).
[16] M. Sundermann, H. Hahn, D. S. Christovam, M. W. Haverkort, R. Caciuffo, B. Keimer, L. H. Tjeng, A. Severing, and H. Gretarsson, Phys. Rev. Res. **7**, 043081 (2025).
[17] J. C. Védrine, Catalysts **7**, 341 (2017).
[18] F. M. F. de Groot, Coord. Chem. Rev. **249**, 31 (2005).
[19] A. Kotani and S. Shin, Rev. Mod. Phys. **73**, 203 (2001).
[20] F. Aquilante, J. Autschbach, A. Baiardi, S. Battaglia, V. A. Borin, L. F. Chibotaru, I. Conti, L. De Vico, M. Delcey, I. Fdez. Galván, N. Ferré, L. Freitag, M. Garavelli, X. Gong, S. Knecht, E. D. Larsson, R. Lindh, M. Lundberg, P. A. Malmqvist, A. Nenov, J. Norell, M. Odelius, M. Olivucci, T. B. Pedersen, L. Pedraza-González, Q. M. Phung, K. Pierloot, M. Reiher, I. Schapiro, J. Segarra-Martí, F. Segatta, L. Seijo, S. Sen, D.-C. Sergentu, C. J. Stein, L. Ungur, M. Vacher, A. Valentini, and V. Veryazov, J. Chem. Phys. **152**, 214117 (2020).
[21] F. Neese, WIRES Comput. Molec. Sci. **2**, 73 (2012).
[22] G. Li Manni, I. Fdez. Galván, A. Alavi, F. Aleotti, F. Aquilante, J. Autschbach, D. Avagliano, A. Baiardi, J. J. Bao, S. Battaglia, L. Birnoschi, A. Blanco-González, S. I. Bokarev, R. Broer, R. Cacciari, P. B. Calio, R. K. Carlson, R. Carvalho Couto, L. Cerdán, L. F. Chibotaru, N. F. Chilton, J. R. Church, I. Conti, S. Coriani, J. Cuéllar-Zuquin, R. E. Daoud, N. Dattani, P. Decleva, C. de Graaf, M. G. Delcey, L. De Vico, W. Dobrautz, S. S. Dong, R. Feng, N. Ferré, M. Filatov(Gulak), L. Gagliardi, M. Garavelli, L. González, Y. Guan, M. Guo, M. R. Hennefarth, M. R. Hermes, C. E. Hoyer, M. Huix-Rotllant, V. K. Jaiswal, A. Kaiser, D. S. Kaliakin, M. Khamesian, D. S. King, V. Kochetov, M. Krośnicki, A. A. Kumaar, E. D. Larsson, S. Lehtola,

M.-B. Lepetit, H. Lischka, P. López Ríos, M. Lundberg, D. Ma, S. Mai, P. Marquetand, I. C. D. Merritt, F. Montorsi, M. Mörchen, A. Nenov, V. H. A. Nguyen, Y. Nishimoto, M. S. Oakley, M. Olivucci, M. Oppel, D. Padula, R. Pandharkar, Q. M. Phung, F. Plasser, G. Raggi, E. Rebolini, M. Reiher, I. Rivalta, D. Roca-Sanjuán, T. Romig, A. A. Safari, A. Sánchez-Mansilla, A. M. Sand, I. Schapiro, T. R. Scott, J. Segarra-Martí, F. Segatta, D.-C. Sergentu, P. Sharma, R. Shepard, Y. Shu, J. K. Staab, T. P. Straatsma, L. K. Sørensen, B. N. C. Tenorio, D. G. Truhlar, L. Ungur, M. Vacher, V. Veryazov, T. A. Voß, O. Weser, D. Wu, X. Yang, D. Yarkony, C. Zhou, J. P. Zobel, and R. Lindh, J. Chem. Theory Comput. **19**, 6933 (2023).

[23] R. Polly, B. Schacherl, J. Rothe, and T. Vitova, Inorg. Chem. **60**, 18764 (2021).

[24] Y. Joly, S. Di Matteo, and O. Bunău, Eur. Phys. J. Spec. Top. **208**, 21 (2012).

[25] O. Bunău and Y. Joly, J. Phys.: Condens. Matter **21**, 345501 (2009).

[26] A. Kotani, AIP Conf. Proc. **652**, 338 (2003).

[27] G. Döring, C. Sternemann, A. Kaprolat, A. Mattila, K. Hämäläinen, and W. Schülke, Phys. Rev. B **70**, 085115 (2004).

[28] R. A. Gordon, M. W. Haverkort, S. S. Gupta, and G. A. Sawatzky, J. Phys.: Conf. Ser. **190**, 012047 (2009).

[29] G. Chabot-Couture, J. N. Hancock, P. K. Mang, D. M. Casa, T. Gog, and M. Greven, Phys. Rev. B **82**, 035113 (2010).

[30] M. Kang, J. Pelliciari, Y. Krockenberger, J. Li, D. E. McNally, E. Paris, R. Liang, W. N. Hardy, D. A. Bonn, H. Yamamoto, T. Schmitt, and R. Comin, Phys. Rev. B **99**, 045105 (2019).

[31] B. T. Chiogo, J. Okamoto, J.-H. Li, T. Ohkochi, H.-Y. Huang, D.-J. Huang, C.-T. Chen, C.-N. Kuo, C.-S. Lue, A. Chainani, and D. Malterre, Phys. Rev. B **106**, 075141 (2022).

[32] G. Krieger, L. Martinelli, S. Zeng, L. E. Chow, K. Kummer, R. Arpaia, M. Moretti Sala, N. B. Brookes, A. Ariando, N. Viart, M. Salluzzo, G. Ghiringhelli, and D. Preziosi, Phys. Rev. Lett. **129**, 027002 (2022).

[33] M. van Veenendaal, Phys. Rev. Lett. **96**, 117404 (2006).

[34] P. Carra, M. Fabrizio, and B. T. Thole, Phys. Rev. Lett. **74**, 3700 (1995).

[35] M. Nakazawa, H. Ogasawara, and A. Kotani, J. Phys. Soc. Jpn. **69**, 4071 (2000).

[36] A. Juhin, C. Brouder, and F. de Groot, Cent. Eur. J. Phys. **12**, 323 (2014).

[37] M. O. J. Y. Hunault, T. G. Burrow, F. Besnard, A. Juhin, and C. Brouder, Angular dependence and powder average of resonant inelastic x-ray scattering (2025), arXiv:2510.20731 [cond-mat.mtrl-sci].

[38] M. Tagliavini, F. Wenzel, and M. W. Haverkort, Polarization dependency in resonant inelastic x-ray scattering (2025), arXiv:2510.12891v1 [cond-mat.mtrl-sci].

[39] J. J. Sakurai, *Advanced Quantum Mechanics* (Addison-Wesley, Reading, Massachusetts, 1967).

[40] R. D. Peacock and B. Stewart, J. Phys. Chem. B **105**, 351 (2001).

[41] L. J. P. Ament, M. van Veenendaal, T. P. Devereaux, J. P. Hill, and J. van den Brink, Rev. Mod. Phys. **83**, 705 (2011).

[42] M. A. Rashid, F. Ahmad, and N. Amir, Int. J. Theor. Phys. **50**, 479 (2011).

[43] J.-H. Ee, D.-W. Jung, U.-R. Kim, and J. Lee, Eur. J. Phys. **38**, 025801 (2017).

[44] D. L. Andrews and T. Thirunamachandran, J. Chem. Phys. **67**, 5026 (1977).

[45] D. L. Andrews and W. A. Ghoul, J. Phys. A: Math. Gen. **14**, 1281 (1981).

[46] C. Brouder, A. Juhin, A. Bordage, and M.-A. Arrio, J. Phys.: Condens. Matter **20**, 455205 (2008).

[47] P. Carra, A. Jerez, and I. Marri, Phys. Rev. B **67**, 045111 (2003).

[48] P. Glatzel, A. Harris, P. Marion, M. Sikora, T.-C. Weng, C. Guilloud, S. Lafuerza, M. Rovezzi, B. Detlefs, and L. Ducotté, J. Synchrotron Rad. **28**, 362 (2021).

[49] M. Retegan, DAXS: Data analysis for x-ray spectroscopy, `https://gitlab.esrf.fr/spectroscopy/daxs` (2025), accessed: 2025-10-20.

[50] I. Fdez. Galván, M. Vacher, A. Alavi, C. Angeli, F. Aquilante, J. Autschbach, J. J. Bao, S. I. Bokarev, N. A. Bogdanov, R. K. Carlson, L. F. Chibotaru, J. Creutzberg, N. Dattani, M. G. Delcey, S. S. Dong, A. Dreuw, L. Freitag, L. M. Frutos, L. Gagliardi, F. Gendron, A. Giussani, L. González, G. Grell, M. Guo, C. E. Hoyer, M. Johansson, S. Keller, S. Knecht, G. Kovačević, E. Källman, G. Li Manni, M. Lundberg, Y. Ma, S. Mai, J. P. Malhado, P. Å. Malmqvist, P. Marquetand, S. A. Mewes, J. Norell, M. Olivucci, M. Oppel, Q. M. Phung, K. Pierloot, F. Plasser, M. Reiher, A. M. Sand, I. Schapiro, P. Sharma, C. J. Stein, L. K. Sørensen, D. G. Truhlar, M. Ugandi, L. Ungur, A. Valentini, S. Vancoillie, V. Veryazov, O. Weser, T. A. Wesołowski, P.-O. Widmark, S. Wouters, A. Zech, J. P. Zobel, and R. Lindh, J. Chem. Theory Comput. **15**, 5925 (2019).

[51] E. Kümmerle and G. Heger, J. Solid State Chem. **147**, 485 (1999).

[52] S. Derenzo, M. Klintenberg, and M. Weber, J. Chem. Phys. **112**, 2074 (2000).

[53] M. Klintenberg, S. Derenzo, and M. Weber, Comput. Phys. Commun. **131**, 120 (2000).

[54] J. L. Pascual, L. Seijo, and Z. Barandiarán, J. Chem. Phys. **98**, 9715 (1993).

[55] M. A. Nygren, L. G. M. Pettersson, Z. Barandiarán, and L. Seijo, J. Chem. Phys. **100**, 2010 (1994).

[56] F. Gendron and J. Autschbach, J. Phys. Chem. Lett. **8**, 673 (2017).

[57] B. O. Roos, The complete active space self-consistent field method and its applications in electronic structure calculations, in *Advances in Chemical Physics* (John Wiley & Sons, Ltd, 1987) Chap. 69, pp. 399–445.

[58] B. O. Roos, P. R. Taylor, and P. E. Sigbahn, Chem. Phys. **48**, 157 (1980).

[59] P. Siegbahn, A. Heiberg, B. Roos, and B. Levy, Phys. Scr. **21**, 323 (1980).

[60] P. E. M. Siegbahn, J. Almlöf, A. Heiberg, and B. O. Roos, J. Chem. Phys. **74**, 2384 (1981).

[61] P. A. Malmqvist, A. Rendell, and B. O. Roos, J. Phys. Chem. **94**, 5477 (1990).

[62] M. Douglas and N. M. Kroll, Ann. Phys. **82**, 89 (1974).

[63] B. A. Hess, Phys. Rev. A **32**, 756 (1985).

[64] B. A. Hess, Phys. Rev. A **33**, 3742 (1986).

[65] A. Wolf, M. Reiher, and B. A. Hess, J. Chem. Phys. **117**, 9215 (2002).

[66] T. B. Pedersen, F. Aquilante, and R. Lindh, Theor. Chem. Acc. **124**, 1 (2009).

[67] K. G. Dyall and K. Fægri, Chem. Phys. Lett. **201**, 27 (1993).
[68] P. Åke Malmqvist, B. O. Roos, and B. Schimmelpfennig, Chem. Phys. Lett. **357**, 230 (2002).
[69] S. Zhang, Polarixs: A python package for angular and polarization dependent rixs convolution, `https://github.com/ZhangHMDS/Polarixs` (2025), accessed: 2025-08-27.
[70] D.-C. Sergentu, C. H. Booth, and J. Autschbach, Chem. Eur. J **27**, 7239 (2021).
[71] D.-C. Sergentu and J. Autschbach, Dalton Trans. **51**, 1754 (2022).
[72] A. Kotani, K. O. Kvashnina, S. M. Butorin, and P. Glatzel, Eur. Phys. J. B **85**, 257 (2012).
[73] J. van den Brink and M. van Veenendaal, J. Phys. Chem. Solids **66**, 2145 (2005).